The pneumococcal iron uptake protein A (PiuA) specifically recognizes tetradentate Fe[III] *bis-* and mono-catechol complexes

Yifan Zhang[1,2], Katherine A. Edmonds[1], Daniel J. Raines[4], Brennan A. Murphy[1], Hongwei Wu[1], Chuchu Guo[3], Elizabeth M. Nolan[3], Michael S. VanNieuwenhze[1], Anne-K. Duhme-Klair[4] and David P. Giedroc[1,2]

[1]Department of Chemistry, Indiana University, Bloomington, IN 47405-7102 USA

[2]Department of Molecular and Cellular Biochemistry, Indiana University, Bloomington, IN 47405 USA

[3]Department of Chemistry, Massachusetts Institute of Technology, Cambridge, MA 02139 USA

[4]Department of Chemistry, University of York, Heslington, York YO10 5DD, United Kingdom

Correspondence to David P. Giedroc: giedroc@indiana.edu

Abstract

Streptococcus pneumoniae (Spn) is an important Gram-positive human pathogen that causes millions of infections worldwide with an increasing occurrence of antibiotic resistance. Fe acquisition is a crucial virulence determinant in *Spn*; further, *Spn* relies on exogenous Fe^{III}-siderophore scavenging to meet nutritional Fe needs. Recent studies suggest that the human catecholamine stress hormone, norepinephrine (NE), facilitates Fe acquisition in *Spn* under conditions of transferrin-mediated Fe starvation. Here we show that the solute binding lipoprotein PiuA from the *piu* Fe acquisition ABC transporter PiuBCDA, previously described as an Fe-hemin binding protein, binds tetradentate catechol Fe^{III} complexes, including NE and the hydrolysis products of enterobactin. Two protein-derived ligands (H238, Y300) create a coordinately-saturated Fe^{III} complex, which parallel recent studies in the Gram-negative intestinal pathogen *Campylobacter jejuni*. Our *in vitro* studies using NMR spectroscopy and ^{54}Fe LC-ICP-MS confirm the Fe^{III} can move from transferrin to apo-PiuA in a NE-dependent manner. Structural analysis of PiuA Fe^{III}-*bis*-catechol and Ga^{III}-*bis*-catechol and Ga^{III}-$(NE)_2$ complexes by NMR spectroscopy reveals only localized structural perturbations in PiuA upon ligand binding, largely consistent with recent descriptions of other solute binding proteins of type II ABC transporters. We speculate that tetradentate Fe^{III} complexes formed by mono- and *bis*-catechol species are important Fe sources in Gram-positive human pathogens, since PiuA functions in the same way as SstD from *Staphylococcus aureus*.

Introduction

Iron is a biologically important transition metal that plays essential roles in respiration, energy metabolism and other cellular processes using oxidation-reduction, electron transfer, and oxygen activation reactions [1]. The sequestration of this essential nutrient from bacterial invaders by the vertebrate host is a central feature of nutritional immunity [2-5]. Host cells deplete labile iron in the serum by secreting high affinity iron-binding proteins such as transferrin, lactoferrin, and ferritin thus inducing widespread iron starvation in invading pathogens [6]. In response to low iron bioavailability, many pathogens synthesize and secrete low molecular weight, high-affinity iron chelators, called siderophores, to scavenge ferric iron (Fe^{III}) from the host environment and subsequently import Fe^{III}-siderophores via specialized high-affinity uptake systems [7-9]. This process of iron acquisition enhances the virulence of many bacterial pathogens during infections, and has been extensively investigated for decades due to its physiological and therapeutic importance [6,10-13].

Streptococcus pneumoniae (Spn) is a commensal inhabitant of the upper respiratory tract in humans, but upon invasion of other sterile tissues becomes a formidable pathogen that causes millions of infections worldwide, many with increasing occurrence of antibiotic resistance [14,15]. *Spn* is a Gram-positive lactic acid bacterium that lacks a TCA cycle and a respiratory electron transfer chain, and thus is characterized by a relatively low cellular Fe quota [16]. In fact, *Spn* has very few known Fe-requiring enzymes and lacks Fur and IdeR, well-characterized global Fe-uptake regulators associated with many Gram-positive and Gram-negative bacteria [17]. Fe homeostasis in *Spn* is instead controlled in part by RitR, an orphan response regulator that senses reactive oxygen species (ROS) generated by cell-excess Fe^{II} and endogenous hydrogen peroxide generated by pyruvate oxidase (SpxB) and lactate oxidase (LctO) when this facultative anaerobe respires on molecular oxygen [16,18,19].

3

Despite what appears to be a low Fe requirement, *Spn* still faces the challenge of acquiring sufficient Fe from the host to meet cellular needs, which becomes particularly critical when *Spn* moves from the upper airway to sterile sites in the lung, cardiac tissue and the bloodstream to cause invasive disease [14,15,20]. No siderophore biosynthesis pathway has been identified in the *Spn* genome and thus it is widely believed that *Spn* is unable to synthesize siderophores [21]. The genome of *Spn* does encode several cell membrane-tethered substrate binding proteins (SBPs) coupled to ATP-dependent active transport systems, as classical ATP-binding cassette (ABC) transporters. Three ABC transporters are known or projected to transport Fe^{III}-siderophores, Pit, Pia, Piu, and two additional iron substrate binding proteins may play an accessory role in Fe uptake [20-24]. It is unknown whether Fe^{II} can be imported by *S. pneumoniae*: although other streptococci encode FeoB, the model serotype 2 *Spn* strain used here, *S. pneumoniae* D39, does not. Only Pia has been biochemically and functionally characterized as an Fe^{III}-ferrichrome uptake transporter in *Spn*, with the physiological Fe substrates for the other systems unclear or unknown [20,25].

The sources of Fe that are bioavailable to *Spn* during colonization or systemic infection are poorly understood. For example, no Fe^{III}-catecholate complex uptake system has been reported in *Spn*, yet previous work reveals that the stress hormone and catecholamine norepinephrine (NE), abundant in the lung, facilitates Fe uptake by *Spn* in human serum when transferrin is the sole iron source [26,27]. Here, NE is thought to function as a catecholate pseudo-siderophore capable of removing Fe^{III} from transferrin [28,29]. NE-stimulated growth stimulation has also been reported in another Gram-positive pathogen, *Staphylococcus aureus*, which expresses an Fe^{III}-catecholate binding protein SstD [30]. *Spn* PiuA is evolutionarily related to *S. aureus* SstD (Fig. 1a), and both are cluster A SBPs belonging to the type II ABC transporters [31]. Type II ABC transporters employ exclusively cluster A SBPs and import metal ions, including Zn^{II} and Mn^{II} (with cluster A-I

4

SBPs), and metal complexes such as Fe^{III}-siderophores, hemin and vitamin B_{12} (with cluster A-II SBPs) [32-37]. Cluster A SBPs consist of N- and C-terminal α/β lobes connected by a single rigid α-helix or brace helix. This contrasts with more extensively studied SBPs belonging to type I transporters. These SBPs have more flexible linkers and bind substrate using a "venus flytrap" mechanism, in which the substrate brings the N- and C-terminal lobes together to promote SBP binding to the permease and substrate transfer. Type II ABC transporters appear to operate quite differently from type I, from substrate binding to ATP hydrolysis [38]. Cluster A SBPs are generally more rigid and bind tightly to the permease in the absence of substrate, while the ATPase components exhibit significant basal hydrolysis activity. These features are thought to optimize the transporter for import of scarce nutrients [39]; however, common mechanistic features of cluster A SBPs remain elusive.

In this study, we redefine *S. pneumoniae* PiuA as an Fe^{III}-tetradentate catecholate binding protein rather than a hemin binding protein, as originally suggested on the basis of limited data [22,40]. Two protein-derived ligands from the central cavity between the N- and C-terminal lobes (H238 and Y300 in PiuA) complete the hexadentate, octahedral Fe^{III} coordination geometry, largely as previously described for periplasmic SBP, CeuE, from the Gram-negative intestinal pathogen *Campylobacter jejuni* [41-43]. This finding expands the known bioavailable iron sources for *Spn* to include both catecholate-type siderophores and hydroxamate-type siderophores. We likewise establish that *S. aureus* SstD is a specific and high affinity receptor for the same coordinately unsaturated Fe^{III}-catecholates [30]. A comprehensive evaluation of the structural and dynamic changes that occur in PiuA in solution upon ligand binding reveals only small, local perturbations in structure consistent with cluster A-II metal-binding SBPs, accompanied by a small increase in localized conformational disorder on the μs-ms time scale upon ligand binding, which may impact Fe^{III}

transport. The implications of these findings on the use of host-endogenous catecholamines as Fe^{III} sources by a respiratory pathogen are discussed.

Results

Pneumococcal PiuA and *Sa*SstD form Fe^{III} tetradentate coordination complexes

PiuA resembles other SBPs that bind tetracoordinate catecholate siderophores

The PiuBCDA ABC transporter system has long been thought to function in heme uptake, but this notion was based on limited biological evidence [19,20,22,40]. Recent studies on the catecholate siderophore binding protein CeuE from *Campylobacter jejuni* suggest that PiuA might instead be specific for coordinately unsaturated catecholate iron complexes [41]. CeuE binds Fe^{III}-enterobactin (Ent) weakly, but has higher affinity (≥100-fold) for the Fe^{III} complexes of the coordinately unsaturated Ent hydrolysis products, including Fe^{III}–di-DHBS (*bis*-2,3-dihydroxybezoyl-L-Ser) or Fe^{III}–DHBS$_2$ (dihydroxy-benzoyl-L-Ser). Crystal structures of CeuE bound to a 1:1 Fe^{III}:di-DHBS complex reveal that the two open Fe^{III} coordination sites on one side of the *bis*-catecholate chelate, conserved among a subset of related SBPs, including tyrosine (Y288) buried in the binding cavity, and histidine (H227) on a flexible, surface loop, coordinate the Fe^{III} [41]. In similar fashion, *Vibrio cholerae* VctP, a CeuE homolog, coordinates the Fe^{III}-tetradentate *bis*-catecholate siderophore salmochelin S1, a hydrolysis product of salmochelin, a C5-glucosylated analog of Ent, using the same tyrosine and histidine residues [43]. The sequence- and structural alignments of PiuA, SstD, CeuE and VctP reveal that the ligating His and Tyr of CeuE are invariant (Fig. 1a,b), as are three arginine residues that create a positively-charged binding cleft characteristic of catecholate-binding SBPs, but not of hemin-binding SBPs (Fig. 1c) [44]. The sequential and structural similarities strongly predict that coordinatively unsaturated Fe^{III} catecholates are substrates for PiuA rather than hemin.

6

PiuA and SstD bind tightly to dimeric and monomeric catecholate siderophores

To test the hypothesis that PiuA is specific for catecholates, we expressed and purified the soluble domains *S. pneumoniae* PiuA and *S. aureus* SstD by removing the N-terminal membrane anchor, and measured equilibrium binding affinities for heme and a number of preformed Fe^{III}-bound catecholate complexes (Fig. 2a) using quenching of the intrinsic fluorescence as a reporter of ligand binding. These complexes include the macrocyclic, hexadentate catecholate enterobactin (Ent), to tetradentate *bis*-catecholates di-DHBS and the artificial tetradentate catecholate siderophore mimic 4-LICAM, to the bidentate monomeric catechols, DHBS and NE (Fig. 2a). These data demonstrate that Fe^{III} complexes of 4-LICAM and the Ent hydrolysis products DHBS and di-DHBS bind tightly to both proteins, essentially stoichiometrically under these solution conditions, with K_a greater than 10^9 M^{-1} (Fig. 2b-g, Supplementary Fig. 1a-f, Table 1) [41,45]. These K_a values are at least 1000-fold higher than those for hemin or Ent, with $K_a \approx 10^6$ M^{-1} in each case (Fig. 2b-c, Supplementary Fig. 1a-b, Table 1). Binding curves for the Fe^{III} complexes of the two monomeric catechols, DHBS and NE, are also stoichiometric under these conditions (Fig. 2e,g, Supplementary Fig. 1a-f, Table 1). Metal-free NE also binds quite weakly to PiuA, as measured using an NMR-based titration, with $K_a \leq 10^2$ M^{-1} (Supplementary Fig. 2). These results reveal that two Gram-positive SBPs, PiuA and SstD, exhibit Fe^{III}-catecholate substrate specificity profiles similar to that of Gram-negative SBP CeuE [41,43].

The fact that the Fe^{III} complexes of two *bis*-catechols and two monomeric catechols bind stoichiometrically under these conditions suggests that stoichiometry of these complexes would be 1:1:1 for Fe:*bis*-catechol:PiuA and 1:2:1 for Fe:mono-catechol:PiuA (Supplementary Fig. 1g-n). Native electrospray ionization-mass spectrometry (ESI-MS) demonstrates that PiuA forms the expected 1:1:1 complex with Fe^{III}–4-LICAM (Fig. 3a, Table 2), consistent with the titration data (Fig. 2b) and previous structural studies of CeuE [45]. In contrast, when the PiuA Fe^{III}-NE complex is subjected to the same ionization

conditions, we observe a mixture of products, including the expected 1:2:1 Fe^{III}–NE_2:PiuA complex, as well as protein complexes of lower masses, *e.g.*, the 1:1:1 Fe^{III}–NE:PiuA complex, a peak that corresponds to a 1:1:1 Fe^{III}–NE:acetate complex, likely derived from the volatile ammonium acetate buffer, as well as some metal-free apo-PiuA (Fig. 3a). These data show that NE binds to PiuA with the expected 1:2 Fe^{III}–NE_2 stoichiometry but forms a complex that is thermodynamically and/or kinetically labile, and becomes partially dissociated during the evaporation process.

To further explore the stoichiometry of complex formation, we sought to employ ^{19}F NMR spectroscopy and thus synthesized 6-fluoronorepinephrine (6-FNE) (see Supplementary methods). We measured the binding affinity of PiuA for Fe^{III}–6FNE (Fig. 3b) and the ^{19}F NMR spectrum of the isostructural (*vide infra*) and diamagnetic Ga^{III}–6-FNE complex (Fig. 3c). These data reveal that Fe^{III}–6-FNE binds essentially stoichiometrically under these conditions (Fig. 3b) with the Ga^{III}–6-FNE PiuA complex characterized by two major ^{19}F signals of equal intensity and linewidth, which differ from those ^{19}F signals associated with the free 6-FNE ligand and the unbound Ga^{III}-6-FNE complex. The presence of two major PiuA-bound ^{19}F NMR signals vs. one in the free (diastereomeric) ligand, is fully consistent with the presence of two NE molecules in the PiuA–Fe^{III}-NE_2 complex (see Supplemenatry Fig. 1g-n, for structural models of these and related complexes).

The conserved histidine and tyrosine stabilize Fe^{III}-catecholate complexes formed by PiuA and SstD

Based on sequence alignments with CeuE and VctP (Fig. 1a), we anticipated that the conserved His and Tyr in PiuA and SstD would serve as donor atoms to the Fe^{III}–catecholate. To evaluate this notion, we measured the Fe^{III}-ligand binding affinities of the H238L and Y300F mutants of PiuA (Fig. 2b) and the corresponding H260L and Y321F mutants of SstD (Supplementary Fig. 1a-f), using the same series of Fe^{III}-coordinated

8

dimeric and monomeric catecholate complexes employed for the wild-type titrations (Fig. 2a) [41,45]. In both cases, the Y-to-F substitution reduces the binding affinity for 4-LICAM and the Ent hydrolysis products by ≥1000-fold, or to a level comparable to that of heme and Ent; in contrast, the affinity of the Fe^{III}–NE_2 complex falls by ≈100-fold (Table 1). The impact of the H-to-L substitution is less severe, with the affinity for Fe^{III}–4-LICAM complex reduced ≈100-fold, and the affinities of the di-DHBS, DHBS and NE complexes reduced by ≤10-fold (Fig. 2b, Supplementary Fig. 1a-f, Table 1). We hypothesize that loss of the Tyr ligand is more significant since it is buried in the binding cleft (Fig. 1b), whereas the His is positioned on a surface-exposed and flexible hairpin loop, a finding consistent with the NMR dynamics measurements (*vide infra*), and thus may be more readily replaced with a solvent molecule.

Fe^{III}-catecholate binding induces only small perturbations of PiuA and SstD structure

Having established the PiuA Fe^{III}–catecholate specificity profile and stoichiometry, we exploited the high thermodynamic and hydrolytic stability of the Fe^{III}–4-LICAM complex to obtain insights into the structural and dynamical perturbations of ligand binding to PiuA in solution. We also leveraged the non-reducible, diamagnetic Ga^{III}-ligand complexes as structural surrogates for the paramagnetic Fe^{III}-ligand complexes, allowing us to perform comprehensive NMR experiments [46]. The Ga^{III}–4-LICAM complex binds with an affinity that is ≈10-fold lower (Supplementary Fig. 3) but with the same stoichiometry, likely partly attributable to the different acidities of the metal-bound water molecules (log K_{OH} = 11.32 for Fe^{III} compared with 10.91 for Ga^{III}) [47].

NMR chemical shift perturbation mapping and paramagnetic relaxation enhancement (PRE)

Although the 31.4 kDa soluble domain of PiuA is large enough to pose significant challenges for solution NMR studies, multi-dimensional NMR spectra of uniformly deuterated, ^{13}C, ^{15}N-labeled (U-^2H,^{13}C,^{15}N) PiuA back-exchanged into H_2O are of remarkably

high quality, allowing us to obtain nearly complete backbone resonance assignments of the apo-state and PiuA bound to Ga^{III}–4-LICAM [48]. A comparison of the ^{1}H,^{15}N-TROSY spectra of apo- and the Ga^{III}–4-LICAM complex (Supplementary Fig. 4a-b) reveals a single set of resonances in both cases, with small chemical shift perturbations (CSPs) found throughout the spectra. The CSPs are largely localized to a small set of residues and show remarkably little change (Fig. 4). When these CSPs are mapped onto the structure of PiuA from the *S. pneumoniae* Canada MDR_19A strain (PDB 4JCC; which differs in only four residues, see Fig. 1a) [48], the largest perturbations are found in the cleft between the N- and C-terminal lobes, in the immediate vicinity of the bound catecholate predicted by homology to CeuE and related SBPs (Fig. 4b). In particular, in the β4-η2, η2-α2, and β6-α3 loops in the N-terminal lobe, and the α5-β8, β10-β11, and α7-β12 loops in the C-terminal lobe. Notably, there is negligible change in chemical shifts in the α5 bridging helix, consistent with the idea that Ga^{III}–4-LICAM binding does not induce a change in the relative orientation of the N- and C-terminal lobes. In fact, the observed CSPs derive primarily from physical proximity to the Ga^{III}–4-LICAM since analyses of the backbone and Cβ chemical shifts as well as amide hydrogen-deuterium exchange (HDX) rates (Supplementary Fig. 5) reveal that the secondary structure in PiuA is not strongly perturbed by Ga^{III}–4-LICAM coordination [48]. The few amides that show decreased HDX rates upon ligand binding are either immediately adjacent to the Fe^{III}-coordinating residue Y300, directly contacted by the loop containing the metal-coordinating residue H238, or very near a conserved catecholate-coordinating arginine.

We also examined the spectral perturbations associated with coordination of the Ga^{III}–NE$_2$, Ga^{III}–6-FNE$_2$, and Fe^{III}–NE$_2$ complexes (Supplementary Fig. 4c,e,f) and the Fe^{III}–4-LICAM complex (Supplementary Fig. 6) by PiuA compared to apo- and Ga^{III}–4-LICAM PiuA complexes. In striking contrast to the uniform spectral quality of the PiuA:Ga^{III}–4-

LICAM complex indicative of a single molecular species (Fig. 4a), many of the crosspeaks in 2D $^1H,^{15}N$ TROSY spectra of PiuA:Ga^{III}–NE$_2$ complex are split into multiplets (Supplementary Fig. 5a). This multiplet structure is likely reporting on a number of distinct binding modes in slow chemical exchange with one another, and is potentially consistent with the complexity of the native ESI-MS spectrum of this complex (Fig. 3a). This spectral complexity is also likely exacerbated by the fact that each (diastereomeric) NE molecule is capable of binding to PiuA in multiple orientations, a finding also observed in prior studies of CeuE complexed with Fe^{III}-DHBS$_2$ where one of the two DHBS ligands was bound in two different orientations in different CeuE molecules within the unit cell (Supplementary Fig. 1l-m) [41]. Interestingly, a far more uniform crosspeak pattern is observed in the spectrum of PiuA bound to Ga^{III}–6-FNE$_2$ (Supplementary Fig. 5b), as if the fluorine substitution biases the orientation of each 6-FNE molecule in the binding pocket. Indeed, whereas the 1D ^{19}F NMR spectrum of 6-FNE has a single, sharp peak at –127 ppm, the spectrum of PiuA-bound Ga^{III}–6-FNE consists of a pair of peaks (at –130.1 and –132.2 ppm; Fig. 3c), rather than the four signals expected for two orientations in each of two positions within the binding pocket.

We next compared the $^1H,^{15}N$ TROSY spectra of the PiuA-bound Fe^{III}–4-LICAM vs. PiuA-bound Ga^{III}–4-LICAM (Supplementary Fig. 6) with these spectral changes mapped on the structure of PiuA (Fig. 4c). Careful examination of these data reveals that the two complexes are isostructural, since the crosspeaks that are observable in both complexes overlay exactly with one another. Furthermore, a quantitative analysis of the paramagnetic relaxation enhancement (PRE) induced by the Fe^{III} atom shows a distance-dependent (as $1/r^6$, where r is the distance between the backbone amide bond vector and the Fe^{III} atom) impact on peak heights fully consistent with the metal and catecholate ligand positioned in the cleft between the lobes with minimal change to the global structure of PiuA relative to the crystal structure of the apo-state (Fig. 4a,b).

Global hydrodynamics: Small angle X-ray scattering (SAXS) and HydroNMR

Given the small structural perturbations induced by ligand binding by NMR spectroscopy, we turned to two global hydrodynamics approaches to ascertain any changes in global structure between the apo- and Fe^{III}-4-LICAM bound states of both PiuA and SstD. Investigation by small angle X-ray scattering (Fig. 5, Supplementary Table 1) reveals that the raw X-ray scattering data are very similar to one another in the apo- and ligand-bound states of both PiuA and SstD and are quite similar to the scattering curves calculated from the ligand-free apo-PiuA structure or an SstD model derived from the petrobactin receptor, *Bacillus subtilis* YclQ, respectively (Fig. 5a) [49-51]. The Guinier plots show that both PiuA and SstD are well-folded, monodisperse, and monomeric with statistically indistinguishable radii of gyration (R_g) and overall shapes in the apo- and ligand-bound states (Fig. 5c,d), with the calculated scattering envelopes fully consistent with the known structure of apo-PiuA (Fig. 5e,f).

We also investigated the global structure of PiuA in the apo- and ligand-bound states by quantitatively analyzing the backbone amide ^{15}N R_1 and R_2, longitudinal and transverse relaxation rates, which not only provide information on internal mobility along the backbone (*vide infra*), but also report on the overall rotational dynamics. The R_1 and R_2 data reveal that PiuA tumbles predominantly as a single globular unit in solution with a rotational diffusion tensor and ^{15}N R_2/R_1 ratio fully compatible with those parameters predicted from the crystal structure using hydroNMR [52], both in the apo and ligand-bound states, with minimal difference between the two states (Supplementary Fig. 7). In particular, there is no significant domain reorientation upon ligand binding as was observed for maltose binding protein, a cluster D-I SBP [31] in a type I transporter [53]; in PiuA, bond vectors in both domains that are parallel to the long axis of the protein in the apo state remain parallel to the long axis in the ligand-bound state. Taken collectively, these data reveal that the global hydrodynamic properties of the apo- and ligand-bound are virtually identical at this

12

resolution and no significant changes in overall shape or oligomerization state occur upon Fe^{III}-*bis*-catecholate ligand binding, a finding consistent with reported structures of apo and ligand-bound CeuE [41].

Fe^{III}- and Ga^{III}-catecholate-induced perturbations in PiuA conformational dynamics

Overall, our NMR and SAXS studies show that there are few structural differences between the apo- and Ga^{III}– or Fe^{III}–4-LICAM bound states, and those that are detected appear localized in the immediate vicinity of the metal-chelate binding pocket. This motivated us to explore the role of conformational dynamics in PiuA on a variety of timescales accessible by NMR, namely sub-nanosecond (sub-ns) amide bond vector reorientations as reported by the steady-state heteronuclear ^{15}N{^{1}H} NOE (hNOE), and backbone motions in the µs-ms timescale, using ^{15}N relaxation dispersion experiments. The hNOE data (Fig. 6a-c) demonstrate that the internal mobility of both states on this timescale largely localizes to loops pointing into the ligand binding cleft between the lobes. In particular, the interdomain linker helix α5 displays negligible mobility on the sub-ns timescale, with hNOE values around 0.8 in both the apo- and Ga^{III}–4-LICAM bound states. In contrast, the β7-α4 loop and the long β10-β11 loop containing the metal-coordinating residue H238 exhibit more flexibility in the apo-state relative to the metal-bound state. This observation may be consistent with the relatively high B-factors in the same loops in the crystal structure of the apo-PiuA (Supplementary Fig. 8a). Interestingly, the β10-β11 loop retains significant mobility on this timescale even in the ligand-bound state, consistent with the idea that Fe^{III} coordination by H238 in this loop has a relatively smaller impact on Fe^{III} affinity (Fig. 2).

This anticipated ligand binding-induced quenching of sub-ns mobility by Ga^{III}–4-LICAM is accompanied by an *increase* in mobility on the µs-ms (slow) timescale in the metal

binding site region, particularly in the C-terminal lobe, but also in the β4-η2, β5-α2, and β6-α3 loops in the N-terminal lobe (Fig. 6d-f; Supplementary Fig. 8b). The increase in slow-timescale flexibility is perhaps most striking in the H238-containing β10-β11 loop. This transfer of motions between fast- and slow-motional regimes upon metal binding is not unprecedented [54]. The absence of significant structural differences between the apo- and Fe^{III}– or Ga^{III}–4-LICAM-coordinated PiuAs, coupled with detectable changes in backbone dynamics, suggests an allosteric mechanism that is largely dynamic in nature, rather than one described by a rigid body motion.

NE-mediated Fe^{III} transfer from human transferrin to metal-free PiuA

NMR-based investigations of Fe^{III}- and Ga^{III}-catecholate transfer to PiuA

Previous studies document that NE is capable of removing iron from human transferrin (hTf) [28,29]; however, an acceptor for the NE-bound Fe^{III} has not been identified in *S. pneumoniae*. To determine if PiuA can function directly as a receptor for hTf-bound Fe^{III}, we investigated this process using NMR, ICP-MS, and UV-Vis spectroscopies. The $^1H,^{15}N$-TROSY spectrum of Fe^{III}-NE_2-PiuA is similar to that of Fe^{III}-4LICAM-PiuA and is quite distinct from that of apo-PiuA, and thus can be used to assess Fe^{III} transfer from hTf to PiuA (Fig. 4a, above). The spectrum of ^{15}N Ga^{III}-NE_2 PiuA (Fig. 7a, *cyan;* full spectra shown in Supplementary Fig. 9) shows some heterogeneity, but is similar enough to that with 4-LICAM that the resonance assignments can be inferred from this spectrum. The spectrum of ^{15}N Fe^{III}-NE_2 PiuA is similar to that of ^{15}N Ga^{III}-NE_2 PiuA, but with many crosspeaks broadened beyond detection (Fig. 7b). In this region of the spectrum shown, only T229 is far enough from the Fe^{III} center for the resonance to remain visible. Thus, successful transfer of Ga^{III} or Fe^{III} from hTf should result in spectra resembling those shown in Fig. 7a or Fig. 7b, respectively.

14

In order to assess Ga^{III} transfer from hTf to PiuA, Ga^{III}-hTf was prepared by incubating apo-hTf with excess Ga^{III}-NTA. When excess Ga^{III}-hTf is added to apo-PiuA, no change is observed in the ^{15}N PiuA spectrum (Fig. 7c), indicating that PiuA cannot directly obtain Ga^{III} from hTf. Similarly, no change in the crosspeak positions or linewidths is observed in the ^{15}N PiuA spectrum upon addition of Fe^{III}-hTf in the absence of NE (Fig. 7d), thus revealing no metal transfer and the absence of a tight interaction between hTf and PiuA. The addition of 1 mM NE to the Ga^{III}-hTf:PiuA mixture also results in an NMR spectrum identical to that of ^{15}N apo PiuA, indicating that PiuA cannot obtain Ga^{III} from hTf even in the presence of excess NE and after incubation overnight at 35.0 °C (Fig. 7e). Strikingly, addition of 1 mM NE to the Fe^{III}-hTf:PiuA mixture results in an NMR spectrum that is nearly identical to that of ^{15}N Fe^{III}-NE$_2$ PiuA, indicating that PiuA can obtain Fe^{III} from hTf, but only in the presence of NE (Fig. 7f). The ability of NE to induce Fe^{III} transfer from hTf, but not Ga^{III} transfer, suggests that the ability of iron to access to the Fe^{II} state is important for NE-mediated iron acquisition by PiuA from hTf. This is consistent with a previous EPR study, which showed that removal of iron from transferrin depends on reduction of high affinity ferric iron to low affinity ferrous iron [28]. Moreover, PiuA appears to function as an Fe^{III} trap which prevents the reassociation of Fe^{III} with transferrin.

Electronic absorption and ^{54}Fe LC-ICP-MS analysis of Fe^{III}-catecholate transfer to PiuA

To confirm NE-dependent removal of Fe^{III} from hTF, the reaction observed by NMR was recapitulated in a cuvette and monitored over time by UV-Vis spectroscopy (Supplementary Fig. 10). Fe^{III}-loaded hTf exhibits an intense ligand-to-metal charge transfer band at ≈450 nm [55]; upon addition of NE and apo-PiuA, this charge transfer band decreases and a new absorption band appears at lower energy with a peak maximum at 515 nm, characteristic of the PiuA-Fe^{III}-NE$_2$ complex [56]. The fast phase of this transfer process occurs over tens of minutes (k_1≈0.1 min^{-1}), with the slower phase ≈10-fold slower

and comparable to rate of loss of Fe^{III} from hTf (Supplementary Fig. 10, *inset*). To further

establish that Fe^{III} transfer to apo-PiuA from hTf is a NE-dependent process, we employed

LC (liquid chromatography)-coupled ICP-MS and $^{54}Fe^{III}$-hTf as the iron source to track both

proteins and the metal simultaneously, while avoiding background ^{56}Fe contamination. Apo-

PiuA and $^{54}Fe^{III}$-hTf were mixed in NMR buffer with or without excess NE and the mixtures

chromatographed on a size-exclusion column, while monitoring both ^{54}Fe counts and protein

absorbance (Fig. 8). These experiments reveal that NE is required to observe significant

^{54}Fe transfer from hTf to PiuA.

Discussion

In the work presented here, we extend our molecular-level understanding of nutrient

Fe acquisition in an important respiratory pathogen, *Streptococcus pneumoniae*. We

redefine PiuA, the solute binding lipoprotein of the PiuBCDA ABC transporter, as a

tetradentate Fe^{III}-siderophore binding protein that forms high-affinity ($K \approx 10^9\,M^{-1}$) complexes

with tetradentate *bis*-catecholate Fe^{III} ligand complexes and Fe^{III} complexes formed by two

monomeric catecholate ligands. On the basis of structural comparisons with *C. jejuni* CeuE

and the ligand binding properties of two mutant PiuAs (H238L and Y300F), we conclude that

two Fe^{III} donor atoms derived from the protein, Y300 and H238, complete the octahedral

coordination geometry of the Fe^{III} ion [45]. Fe^{III}-Ent binds far more weakly to PiuA than

complexes formed with *bis*- and monomeric catechols (Table 1). This suggests that intact

enterobactin (Ent) may be a poor transport substrate for PiuBCDA, although it has not yet

been experimentally validated. Our findings also call into question previous work that

suggests that the PiuA transporter functions in heme uptake [22], because hemin binds

weakly to PiuA relative to unsaturated Fe^{III}-catechols. Since *S. pneumoniae* is not known to

encode a *bona fide* heme oxygenase required to access heme Fe, and the electrostatics of

the ligand binding cleft in PiuA are very similar to that of other known catecholate receptors

(Supplementary Fig. 11), the re-assignment of PiuBCDA as an Fe^{III}-catecholate-specific SBP is supported by all of the data presented here [16,45,57].

We further demonstrate that the lipoprotein *S. aureus* SstD of the SstABCD transporter possesses biochemical and structural properties that mirror those of *S. pneumoniae* PiuA, findings consistent with previous biological studies [30]. Interestingly, the Sst transporter in *S. aureus* is just one of three Fe uptake systems that allow *S. aureus* to access the transferrin Fe^{III} pool, with the others being endogenously synthesized carboxylate-type siderophores, staphyloferrin A (SfnA) and staphyloferrin B (SfnB) [30]. SstD is only required for growth of *S. aureus* on Fe^{III}-Tf as the sole Fe source in a double mutant unable to import Fe^{III}-SfnA or Fe^{III}-SfnB, and growth requires the presence of simple catechols NE or Ent hydrolysis products, di-DHBS and DHBS [30]. *S. pneumoniae*, in contrast, is widely believed not to biosynthesize siderophores, and is thus dependent on acquiring Fe^{III} by taking up Fe^{III}-siderophores synthesized by other microbes in polymicrobial communities, *e.g.*, Fe^{III}-ferrichrome complexes via the Pia transporter, or accessing other endogenous catechols in the immediate microenvironment [25].

The natural substrate for PiuA is yet to be determined, and may well vary with colonization niche. We show here that the host-derived endogenous catecholamine NE, highly abundant in the lung, forms a high affinity complex with PiuA, and thus provides a mechanistic explanation for reports of NE-stimulated growth proliferation of *S. pneumoniae* under conditions of Tf-mediated Fe^{III} limitation [7,27,29,58-60]. We provide direct evidence that PiuA functions as an Fe^{III} acceptor or trap for Tf-bound Fe^{III} via the intermediacy of the relatively unstable and exchange-labile Fe^{III}-NE complexes [28], with Ent hydrolysis products expected to function in largely the same way. Although mechanistic details remain unclear, it seems possible that sacrificial auto-oxidation of the catechol moiety of di-DHBS, DHBS or NE may well reduce the Tf-bound Fe^{III} to Fe^{II}, which upon dissociation and re-oxidation is captured by the collaborative action of the SBP (PiuA, SstD) and the catecholates

17

themselves [28,61]. Our NMR studies show that a reduction step is necessary since NE is incapable of transferring Ga^{III}, a redox-inactive, diamagnetic Fe^{III} surrogate, from Ga^{III}-hTf to PiuA. Taken collectively, <mark>these studies suggest that</mark> coordinately unsaturated, rapidly exchanging, thermodynamically unstable (relative to Ent) Fe^{III}–catechol complexes can be exploited as a significant source of nutritional Fe [62].

This work, along with previous work in *S. aureus* [30], establishes that Gram-positive pathogens exploit a mechanism of Fe^{III}-uptake that has only previously been extensively characterized in Gram-negative organisms, notably in the intestinal pathogens, *C. jejuni*, *Vibrio cholerae, E. coli* and *Salmonella enterica* [43,45,63]., In *C. jejuni*, for example, an outer membrane receptor, CfrA, brings Fe^{III}-Ent or Fe^{III}-salmochelin complexes into the periplasm, where periplasm-resident esterases, *e.g.,* Cee in *C. jejuni*, hydrolyze Ent to di-DHBS and DHBS monomers that coordinate Fe^{III} and bind to CeuE for cytoplasmic transport. A similar mechanism is thought to be employed by *V. cholerae* VctP in processing complexes of Fe^{III} and salmochelin hydrolysis products [43,64-67], *e.g.,* salmochelin-S1, a naturally occurring tetradentate siderophore produced by *S. enterica* in the gut [68]. In contrast, in *S. enterica* and *E. coli*, esterases reside in the cytoplasm, not the periplasm. The bioavailability of <mark>bacterially-sourced</mark> Ent and salmochelin hydrolysis products to *S. pneumoniae* is unknown. <mark>The two common commensal co-colonizers of the human nasopharynx, *Haemophilus influenzae* and *Moraxella catarrhalis,* do not synthesize siderophores under conditions of Fe starvation [69-71]. Further, although it was recently reported that *Rothia mucilaginosa,* a common commensal of the oral cavity, synthesizes Ent [72], it is unknown if Ent or Ent hydrolysis products are accessible to *S. pneumoniae* in this and other colonization sites.</mark> Based on the available information, we favor a model in which host-derived endogenous catecholamines or another bacterially derived, naturally occurring tetradentate siderophore(s), are the primary physiological substrates for PiuA. The utilization of these simple catechols as nutritional Fe^{III} sources, of course, requires a catabolic system

to detoxify catechols, which by virtue of their facile auto-oxidation (a key feature of Fe^{III}-hTf uptake) are strong potentiators of oxidative and electrophile stress inside cells [73-77].

Our structural studies of PiuA and SstD reveal that the coordination of Fe^{III}-siderophore results in very small perturbations in the structure that are strongly localized in the cleft between the two lobes. The global hydrodynamic properties of the molecule do not change appreciably, and the secondary structural stability, as measured by H-D exchange, is essentially unaffected. The long brace helix, in particular, that connects to the N- and C-terminal lobes is completely insensitive to ligand binding. This feature of PiuA seems to differ from the Mn^{II}-specific PsaA, another *S. pneumoniae* cluster A SBP lipoprotein, previously investigated by crystallography, EPR spectroscopy, and single-molecule FRET studies [38,78,79], and the bacillibactin (*tris*-catecholate) siderophore binding protein *Bacillus subtilis* FeuA [80,81]. Although we anticipated some plasticity in the ligand binding site in order to accommodate promiscuity among catecholate siderophore substrates, we find that PiuA is surprisingly rigid in solution in both the apo and bound states, with the ligand binding site pre-organized to facilitate high affinity binding and rapid on-rates, appropriate for the capture and transport of scarce, exchange-labile nutrient complexes [39]. Binding promiscuity is likely enabled by the extensive solvent exposure of the ligand binding pocket, and any heterogeneity in complex formation, as observed in the $Ga^{III}–NE_2$ complex, for example, is in slow chemical exchange, and may not significantly interconvert on any appreciable timescale. These structural and dynamical features are largely consistent with other cluster A-II SBPs, including the only other case studied by NMR spectroscopy, *E. coli* FepB [46], which are primarily tasked with the capturing scarce transition metals as metal-ligand complexes and transporting them into the cytoplasm [32-37].

Despite this overall rigidity in solution, the $\beta 10$-$\beta 11$ loop in PiuA harboring the Fe^{III}-coordinating histidine (H238) is quite flexible in the apo- and ligand-bound states in the sub-ns timescale, perhaps consistent with the fact that this residue contributes only an order of

magnitude to the Fe^{III}-binding affinity, while the conserved tyrosine (Y300) accounts for three orders of magnitude. A model of the complete ABC transporter suggests that this loop is near the interface with the transmembrane component, potentially poising it to participate in ligand exchange, facilitating transfer to the permease. Structural work on the complete transporter for vitamin B$_{12}$ in *E. coli,* BtuCD-F, leads us to anticipate that the binding of PiuA to the PiuBC permease heterodimer facilitates release of Fe^{III} in part by slightly spreading the N- and C-terminal lobes of PiuA apart, disrupting the substrate binding pocket, while also displacing the ligand by insertion of helices from the permease into the distorted pocket [82]. Our NMR dynamics studies suggest that if permease binding does induce such a conformational change, it does so by an induced-fit mechanism, rather than by conformational selection, since we do not observe sampling of additional open conformations in the apo state or in the ligand-bound state. ==The exceptional rigidity of PiuA even upon binding substrate likely reflects a pre-organized binding pocket that is optimized to bind scarce substrate with a high on-rate and high affinity, requiring the permease to pull the lobes apart to release the substrate [39].== Future structural and dynamics studies of the intact PiuBCDA transporter will provide significant support for these ideas, using the work reported here as foundation for those studies.

Materials and Methods

Cloning, protein expression, and purification of PiuAs and SstDs

The regions of the genes encoding the soluble, extracellular domain of *S. pneumoniae* D39 PiuA (locus tag SPD_1652 or SPD_RS08740) encompassing residues 37-321 was PCR-amplified from the genomic DNA [83] and the 27-residue N-terminal deletion of SstD (locus tag BN8422_RS03995) was amplified from *Staphylococcus aureus* Newman genomic DNA. Each gene was inserted into the pSUMO expression vector [84] with an N-terminal hexahistidine tag, with mutants prepared by PCR-based site-directed mutagenesis.

The expression vectors were transformed into *E. coli* BL21(DE3) strain and grown in LB medium supplemented with 30 µg/mL kanamycin for biochemical experiments, or in M9 minimal medium containing 1.0 g of $^{15}NH_4Cl$ (Cambridge Isotope Laboratories) as the sole nitrogen source for NMR experiments. 1 mM isopropyl β-*D*-1-thiogalactopyranoside (IPTG) was added to induce protein expression at OD_{600} 0.8. Following overnight expression at 18 °C, the cells were collected by centrifugation. The cell pellet was resuspended in Buffer A (25 mM Tris, 500 mM NaCl, 10% glycerol and 20 mM imidazole, pH 8) and lysed by sonication on ice. The crude lysate was clarified by centrifugation. 70% ammonium sulfate was applied to precipitate the protein and the pellet was collected by centrifugation. The precipitated pellet was resuspended in Buffer A isolated by Ni(II) affinity chromatography using a 5 mL HisTrap FF column (GE Healthcare Life Sciences) with a gradient from 100% buffer A to 100% buffer B (25 mM Tris pH 8.0, 500 mM NaCl, 10% glycerol, and 500 mM imidazole). The fractions with the His-tagged SUMO fusion protein were collected and digested by SUMO protease (20 µg/mL) while dialyzing in buffer A with 2 mM dithiothreitol (DTT) at room temperature. The digested protein fractions were applied to a HisTrap FF column in Buffer A. The flow through was collected and concentrated by centrifugation with a 10 kDa cutoff for size exclusion chromatography on a Superdex-75 column in Buffer C (25 mM Tris pH 8.0, 500 mM NaCl, 2 mM EDTA). PiuA purified in this way was found to have <0.1 molar equivalents of Fe as measured by ICP-MS and was confirmed by to be monomeric by gel filtration chromatography. [PiuA] was measured using the estimated molar extinction coefficient at 280 nm (ε_{280}) of 16,960 M^{-1} cm^{-1} while for SstD, ε_{280} is 20,400 M^{-1} cm^{-1}. Purified protein fractions were collected and stored at –80 °C for further experiments.

Preparation of Fe^{III} complexes of NTA, n-LICAM, Ent, di-DHBS, DHBS, NE and 6-FNE

Enterobactin, di-DHBS and DHBS monomer were synthesized and purified as previously described [85,86]. *4*-LICAM was synthesized as previously described [87,88]. The synthesis of (±)-6-fluoronorepinephrine oxalate (6-FNE) is described in the Supplementary methods. Fe^{III}-ligand complexes were prepared by slight modifications of a literature protocol [42,45]. 20 mM $FeCl_3$ (Sigma-Aldrich, F2877, ≥98%) was prepared in 0.3 M HCl and used directly as the Fe^{III} stock solution. Metal-free ligand stock solutions were prepared via dissolution in neat DMSO to the following concentrations: NTA (Sigma Aldrich N9877), 20 mM; 4-LICAM, 30 mM; di-DHBS, 30 mM; DHBS, 60 mM; (±)-norepinephrine (+)-bitartrate salt (Sigma Aldrich A0937; NE), 60 mM; (±)-6-fluoronorepinephrine oxalate (6-FNE), 60 mM; Ent, 20 mM. The Fe^{III} stock solution and each ligand stock were mixed to 1:1 volume ratio at 25 °C for 1 h to generate Fe^{III}-ligand complexes that are 10 mM in total Fe: Fe^{III}-NTA, Fe^{III}_2-4-LICAM$_3$, Fe^{III}_2-di-DHBS$_3$, Fe^{III}-DHBS$_3$, Fe^{III}-NE$_3$ and Fe^{III}-Ent. We note that only the Fe^{III}-Ent complex forms a clean 1:1 complex under these conditions, whereas the others are mixtures of 1:1 and 3:2 complexes (for tetradentate *bis*-catechols, 4-LICAM and di-DHBS) and likely 1:1 and 2:1 complexes (for bidentate monomeric catechols DHBS, NE and 6-FNE) [42,45]. These mixtures were diluted 20-fold into 50 mM HEPES, pH 7.5, 150 mM NaCl to yield a 0.5 mM Fe^{III}-ligand complex solution which was used directly for all titration and structural studies. For ^{54}Fe transfer experiments (see below), $^{54}Fe_2O_3$ purchased from Cambridge Isotope Laboratories (FELM-3900-PK, chemical purity 98%) and dissolved in 0.3 M HCl to prepare a 20 mM $^{54}FeCl_3$ stock solution. $^{54}Fe^{III}$-NTA and $^{54}Fe^{III}$-NE$_3$ were prepared as described above using $^{54}FeCl_3$ as the iron stock. Ga^{III}-4-LICAM, Ga^{III}-NE$_3$, and Ga^{III}-6FNE$_3$ were prepared using exactly the same protocol as describe for Fe^{III} complexes, except that $GaCl_3$, prepared by dissolving Ga_2O_3 in 0.3 M HCl was used as the gallium stock [48].

Intrinsic tryptophan fluorescence quenching titration analysis

Data were acquired on a PC1 spectrofluorometer with λ_{ex} 278 nm (1 mm slit) and the emission intensity recorded through a 340 nm cut-off filter. The Fe^{III}-ligand complexes prepared as described above to a total Fe^{III} concentration of 20 µM in chelexed titration buffer 50 mM HEPES, pH 7.5, 150 mM NaCl. Fe^{III}-ligand complexes were titrated into 3 mL 200 nM protein in the same buffer from 0 to 1.2 µM Fe^{III} with continuous stirring at 25.0 (±0.1) °C. The total emission fluorescence intensity prior to addition of ligand was assigned a value of 1. All titration data were fit to a 1:1 protein: Fe^{III} binding model to estimate K_a using DynaFit. For Fe^{III}-NE_3 titration, a blank titration of Fe^{III}-NE_3 into buffer was used to correct the raw protein ligand titration curve due to the similar intrinsic fluorescence emission spectra of the Fe^{III}-NE_3 ligand. The normalized I_i for the ith Fe^{III} concentration is defined by eq. 1

$$I_i = I_i^R \Big/ \frac{Int_i^B}{Int_0^B} \qquad (1)$$

where I^R represents the normalized raw fluorescence data, Int^B represent the fluorescence intensity of blank titration, i is the Fe^{III} concentration, 0 represent the initial background fluorescence prior to the start of the titration.

Preparation of holo-PiuA and holo-SstD samples for structural analysis

The Fe^{III}-4-LICAM and Fe^{III}-NE_2 complexes of PiuA and SstD were prepared by addition of a molar excess of Fe^{III} relative to apoprotein as Fe^{III}_2-4-$LICAM_3$ or Fe^{III}-NE_3, in 50 mM HEPES, pH 7.5, 150 mM NaCl. The excess ligand was removed by centrifugation in Amicon Ultra-0.5 10 kDa micro-filtration device. The PiuA complexes formed with Ga^{III}-4-LICAM and Ga^{III}-NE_2 were prepared in the same way.

Native ESI mass-spectrometry

The apo, Fe^{III}-4-LICAM and Fe^{III}-NE_2 binding states of PiuA were buffer exchanged to 500 mM ammonium acetate, pH 7.0 at 30 µM protein, with native electrospray ionization (ESI)-MS scans recorded on a Synapt G2S HDMS instrument, via direct infusion at a flow-rate of 100 µL min^{-1}. Samples were ionized via ESI in positive ion mode, with a source voltage of 2.0 kV. Sampling cone and source offset were set to 40.0 V and 80.0 V, respectively, with source and desolvation temperatures set to 80 °C and 100 °C, respectively. The cone gas flow was 1L h^{-1} and the desolvation gas flow was 600 L h^{-1}, with nebulizer at 5 bar. Mass spectra and mobility distributions were analyzed using Mass Lynx v4.1 and OriginPro 2018.

NMR spectroscopy

NMR samples contained 0.1-0.9 mM PiuA, with 25 mM MES pH 6.5, 150 mM NaCl, and 10% v/v D_2O, with 0.3 mM 2,2-dimethyl-2-silapentanesulfonic acid (DSS) as an internal reference. NMR spectra were recorded at 35.0 °C on a Bruker Avance Neo 600 MHz spectrometer equipped with a cryogenic probe or on a Varian VNMRS 800 MHz spectrometer with a room temperature 5 mm PFG HCN probe in the METACyt Biomolecular NMR Laboratory at Indiana University, Bloomington. Data were collected using Topspin 4.0.7 (Bruker), and processed and analyzed on NMRbox [89], using NMRPipe [90] and NMRFAM Sparky [91], respectively. Chemical shift perturbations (CSP) of the backbone upon ligand binding were calculated using ^1H and ^{15}N chemical shifts with $\Delta\delta=((\Delta\delta H)^2+0.2(\Delta\delta N)^2)^{1/2}$. Chemical shift perturbations upon interaction with NE were monitored using 0.1 mM ^{15}N PiuA and concentrations of NE ranging from 0.05 mM to 12.8 mM.

SAXS data acquisition and analysis

The apo and Fe^{III}-4-LICAM binding states of PiuA and SstD were prepared in 50 mM HEPES, pH 7.5, 150 mM NaCl at three different concentrations (5 mg/mL, 3 mg/mL and 1

mg/mL). The scattering data were obtained at sector 12ID-B at the Advanced Photo Source (APS) at Argonne National Laboratory. The buffer scattering was subtracted from the sample scattering, with modified sample scattering curves merged to generate a scattering curve for further analysis. The scattering data at low q values were used to estimate the radius of gyration (R_g) by the Guinier approximation with the range of $qR_g<1.3$. Theoretical SAXS curves for the apoproteins were calculated using the FoXS Server [92,93] based on the crystal structure of PiuA (PDB code 4JCC) and a SWISS MODEL-generated model [50,94-96] of SstD from *B. subtilis* YclQ (PDB 3GFV) [49]. The model envelopes of apo and ligand binding states of PiuA and SstD were generated by DAMMIF and superimposed with the corresponding apoprotein structural models.

Methods to monitor NE-catalyzed Fe^{III} or Ga^{III} transfer from hTf to PiuA

Preparation of Fe^{III} or Ga^{III} (holo) human transferrin (hTf)

      Metal-free apo hTf was purchased from Sigma Aldrich (T1147) and dissolved directly in chelexed hTf buffer containing 200 mM sodium bicarbonate, pH 7.4, 150 mM NaCl. An Fe^{III}-NTA stock solution was added to apo-hTf to an Fe^{III}:hTf ratio of 4:1 to ensure full iron loading of the two Fe^{iii} binding sites in hTf and incubated 4 h at 4 ºC. The mixture then was dialyzed overnight at 4 °C in hTf buffer with gentle orbital shaking to remove the excess iron to obtain Fe^{III}–hTf and concentrated by Amicon Ultra-0.5 30 kDa micro-filtration device for use. Ga^{III}–hTf was prepared in the same way. The apo-hTf concentration was estimated using a molar extinction coefficient at 280 nm of 11,400 M^{-1} cm^{-1} and a MW of 81,000 Da [97-99].

NMR measurements of metal transfer from Tf to PiuA

      A mixture of 150 μM ^{15}N apo-PiuA and 160 μM Ga^{III}-hTf in NMR buffer (25 mM MES pH 6.5, 150 mM NaCl, 10% v/v D_2O, 0.3mM DSS) was incubated at 35.0 °C and monitored

for evidence of Ga^{III} transfer by a 2D ^{1}H,^{15}N TROSY NMR spectrum. 1 mM NE was added to the NMR tube, and two additional 2D ^{1}H,^{15}N TROSY NMR spectra were recorded, for a total incubation time over 24 h. The same experiment was repeated with approximately 620 µM Fe^{III}-hTf and 700 µM ^{15}N apo-PiuA, with 11-h 2D ^{1}H,^{15}N TROSY NMR spectra recorded before and after addition of 1 mM NE at 35.0 °C. Control 2D ^{1}H,^{15}N TROSY NMR spectra were also recorded of ^{15}N apo-PiuA alone, as well as directly loaded ^{15}N Fe^{III}-NE$_2$-PiuA and ^{15}N Ga^{III}-NE$_2$-PiuA for comparison.

UV-Vis measurement of the kinetics of NE-dependent Fe^{III} transfer from hTf to PiuA

A mixture of 100 µM apo-PiuA and 100 µM ^{54}Fe^{III}-hTf was prepared under aerobic conditions in NMR buffer at 35.0 °C in a capped cuvette, and the changes in absorption monitored in a Agilent Cary 8454 UV-VIS spectrophotometer. UV-Vis absorption spectra were recorded from 400 nm to 800 nm every 1 min following the addition of 1 mM NE. The increase in absorption at 515 nm was monitored as an indicator of the generation of Fe^{III}-NE complexes. The resulting progress curves where individually fit to a single exponential or double exponential model..

LC-ICP-MS analysis of NE-dependent Fe^{III} transfer from Tf to PiuA

200 µM apo-PiuA was mixed with 200 or 100 µM ^{54}Fe-hTf with or without 1 mM NE in NMR buffer at 35.0 °C overnight. Control incubations contained 200 µM apo-PiuA, 200 µM ^{54}Fe^{III}-NE$_2$-PiuA, of 200 µM ^{54}Fe-hTf. An Agilent 1260 Infinity II Bio-Inert LC system was used with the autosampler and column compartment cooled at 4 °C. 100 µL injections were applied to a Bio SEC-3 (Agilent) column at a flow rate of 0.35 mL/min using 200 mM NH$_4$NO$_3$, pH 7.5 as running buffer. UV profiles were monitored at 280 nm, with the flow path immediately diverted to the nebulizer of an Agilent 8800 triple quadrupole ICP-MS operating

in He collision mode to detect ^{54}Fe counts. The ^{54}Fe counts were normalized to the maximum count in each spectrum.

^{15}N spin relaxation experiments

^{15}N spin relaxation rates, R_1 and R_2, and ^{1}H-^{15}N heteronuclear NOE (hNOE) values were measured using TROSY pulse sequences [100]. The relaxation delays used were 0.05, 0.20, 0.50, 0.80, 1.2, 1.6, 2.0, and 2.5 s for R_1 and 0.017, 0.034, 0.051, 0.068, 0.085, 0.102, 0.119, 0.136, 0.170, and 0.204 s for R_2. Residue-specific R_1 and R_2 values were obtained from fits of peak intensities vs. relaxation time to a single exponential decay function, while hNOE ratios were ascertained directly from intensities in experiments recorded with (2 s relaxation delay followed by 3 s saturation) and without saturation (relaxation delay of 5 s). Errors in hNOE values were calculated by propagating the error from the signal to noise. The results for both samples were in very good agreement with the relaxation rates obtained from HydroNMR [52] using the crystal structure of *S. pneumoniae* Canada MDR_19A strain apo-PiuA (PDB 4JCC). A value of the atomic radius element of 3.2 Å, the known viscosity for water at 35°C [101], and CSA of -120 ppm were used for this calculation. Relaxation dispersion measurements were acquired using a ^{1}H, ^{15}N TROSY adaptation of a Carr–Purcell–Meiboom–Gill (CPMG) pulse sequence [102]. Experiments were performed at 35.0 °C at 600 MHz with CPMG field strengths (v_{CPMG}) of 25, 50, 100, 250, 500, 750, and 1,000 Hz, with 50 and 500 Hz collected in duplicate. Peak intensities in CPMG experiments were converted to effective transverse relaxation rates ($R_{2,eff}$) using the equation, $R_{2,eff} = (-1/T) \ln(I/I_0)$, where I and I_0 are peak intensities measured with and without the CPMG delay [103]. Errors were propagated from the signal to noise ratio using Monte-Carlo simulations.

1D ^{19}F NMR spectroscopy

Samples for 1D ^{19}F NMR spectroscopy contained NMR buffer (25 mM MES pH 6.5, 150 mM NaCl, 10% v/v D_2O, 0.3 mM DSS), with 30 µM trifluoroacetic acid (TFA) as an internal reference frequency standard. Samples contained 0.3 mM 6-FNE alone, 0.3 mM 6-FNE with 0.35 mM GaCl$_3$, or 1 mM PiuA fully loaded with an excess of 6-FNE and GaCl$_3$ and washed extensively in NMR buffer with TFA. Spectra were recorded for 2-9 h. 1D ^{19}F spectra were processed and analyzed using MestReNova (Mestrelab Research).

Hydrogen-deuterium exchange (HDX) monitored by NMR spectroscopy

Samples containing 0.3 mL of 0.45 mM ^{15}N apo-PiuA or Ga^{III}–4-LICAM-PiuA in NMR buffer (25 mM MES pH 6.5, 150 mM NaCl, 0.3 mM DSS) were lyophilized. Each sample was resuspended in fresh D_2O immediately prior to recording a series of 40-minute ^{1}H,^{15}N TROSY spectra to monitor the disappearance of crosspeaks.

Accession Numbers

Measured relaxation rates have been deposited to the BMRB with accession numbers 50332 and 50333, for apo- and Ga^{III}–4-LICAM PiuA, respectively.

CRediT authorship contribution statement

Y.Z. and D.P.G. conceptualized the study, and Y.Z., K.A.E. and D.P.G. wrote the manuscript. Y.Z. performed all biochemical experiments and K.A.E. acquired all NMR data, some with the assistance of H.W., and K.A.E. processed and analyzed all NMR data of PiuA complexes. D.J.R. synthesized the 4-LICAM under the supervision of A.K.D.-K., B.M. synthesized the 6-fluoronorepinephrine under the direction of M.S.V., and C.G. purified Ent and prepared the Ent hydrolysis products under the supervision of E.M.N. All co-authors were asked to provide editorial comments on the manuscript.

Acknowledgements

Appendix A. Supplementary data

Supplementary data to this article can be found online at

https://doi.org/10.1016/j.jmb.2020.xy.xyz

Keywords

Iron uptake; solute binding protein; *Streptococcus pneumoniae*; catechol; siderophore

References

[1]   Andreini, C., Putignano, V., Rosato, A., Banci, L., (2018). The human iron-proteome. *Metallomics*, **10**, *1223-1231*, *https://doi.org/10.1039/c8mt00146d*.
[2]   Weinberg, E.D., (1975). Nutritional Immunity - Hosts Attempt to Withhold Iron from Microbial Invaders. *J Am Med Assoc*, **231**, *39-41*, *https://doi.org/DOI 10.1001/jama.231.1.39*.
[3]   Hood, M.I., Skaar, E.P., (2012). Nutritional immunity: transition metals at the pathogen-host interface. *Nat Rev Microbiol*, **10**, *525-537*, *https://doi.org/10.1038/nrmicro2836*.
[4]   Bilitewski, U., Blodgett, J.A.V., Duhme-Klair, A.K., Dallavalle, S., Laschat, S., Routledge, A., Schobert, R., (2017). Chemical and Biological Aspects of Nutritional Immunity-Perspectives for New Anti-Infectives that Target Iron Uptake Systems. *Angew Chem Int Ed Engl*, **56**, *14360-14382*, *https://doi.org/10.1002/anie.201701586*.
[5]   Nunez, G., Sakamoto, K., Soares, M.P., (2018). Innate Nutritional Immunity. *J Immunol*, **201**, *11-18*, *https://doi.org/10.4049/jimmunol.1800325*.

[6] Wooldridge, K.G., Williams, P.H., (1993). Iron uptake mechanisms of pathogenic bacteria. *FEMS Microbiol Rev*, **12**, *325-348*,

[7] Saha, R., Saha, N., Donofrio, R.S., Bestervelt, L.L., (2013). Microbial siderophores: a mini review. *J Basic Microbiol*, **53**, *303-317*, *https://doi.org/10.1002/jobm.201100552*.

[8] Kramer, J., Ozkaya, O., Kummerli, R., (2020). Bacterial siderophores in community and host interactions. *Nat Rev Microbiol*, **18**, *152-163*, *https://doi.org/10.1038/s41579-019-0284-4*.

[9] Hider, R.C., Kong, X., (2010). Chemistry and biology of siderophores. *Nat Prod Rep*, **27**, *637-657*, *https://doi.org/10.1039/b906679a*.

[10] Chao, A., Sieminski, P.J., Owens, C.P., Goulding, C.W., (2019). Iron Acquisition in Mycobacterium tuberculosis. *Chem Rev*, **119**, *1193-1220*, *https://doi.org/10.1021/acs.chemrev.8b00285*.

[11] Marchetti, M., De Bei, O., Bettati, S., Campanini, B., Kovachka, S., Gianquinto, E., Spyrakis, F., Ronda, L., (2020). Iron Metabolism at the Interface between Host and Pathogen: From Nutritional Immunity to Antibacterial Development. *Int J Mol Sci*, **21**, *https://doi.org/10.3390/ijms21062145*.

[12] Kirienko, D.R., Kang, D., Kirienko, N.V., (2018). Novel Pyoverdine Inhibitors Mitigate Pseudomonas aeruginosa Pathogenesis. *Front Microbiol*, **9**, *3317*, *https://doi.org/10.3389/fmicb.2018.03317*.

[13] Robinson, A.E., Heffernan, J.R., Henderson, J.P., (2018). The iron hand of uropathogenic Escherichia coli: the role of transition metal control in virulence. *Future Microbiol*, **13**, *745-756*, *https://doi.org/10.2217/fmb-2017-0295*.

[14] Lynch, J.P., 3rd, Zhanel, G.G., (2010). Streptococcus pneumoniae: epidemiology and risk factors, evolution of antimicrobial resistance, and impact of vaccines. *Curr Opin Pulm Med*, **16**, *217-225*, *https://doi.org/10.1097/MCP.0b013e3283385653*.

[15] Marks, L.R., Davidson, B.A., Knight, P.R., Hakansson, A.P., (2013). Interkingdom signaling induces *Streptococcus pneumoniae* biofilm dispersion and transition from asymptomatic colonization to disease. *mBio*, **4**, *https://doi.org/10.1128/mBio.00438-13*.

[16] Lisher, J.P., Tsui, H.T., Ramos-Montanez, S., Hentchel, K.L., Martin, J.E., Trinidad, J.C., Winkler, M.E., Giedroc, D.P., (2017). Biological and Chemical Adaptation to Endogenous Hydrogen Peroxide Production in *Streptococcus pneumoniae* D39. *mSphere*, **2**, *e00291-16 https://doi.org/10.1128/mSphere.00291-16*.

[17] Pinochet-Barros, A., Helmann, J.D., (2017). Redox Sensing by Fe(2+) in Bacterial Fur Family Metalloregulators. *Antioxid Redox Signal*, **29**, *1858–1871 https://doi.org/10.1089/ars.2017.7359*.

[18] Glanville, D.G., Han, L., Maule, A.F., Woodacre, A., Thanki, D., Abdullah, I.T., Morrissey, J.A., Clarke, T.B., Yesilkaya, H., Silvaggi, N.R., Ulijasz, A.T., (2018). RitR is an archetype for a novel family of redox sensors in the streptococci that has evolved from two-component response regulators and is required for pneumococcal colonization. *PLoS Pathog*, **14**, *e1007052*, *https://doi.org/10.1371/journal.ppat.1007052*.

[19] Ulijasz, A.T., Andes, D.R., Glasner, J.D., Weisblum, B., (2004). Regulation of iron transport in Streptococcus pneumoniae by RitR, an orphan response regulator. *J Bacteriol*, **186**, *8123-8136*, *https://doi.org/10.1128/JB.186.23.8123-8136.2004*.

[20] Brown, J.S., Gilliland, S.M., Holden, D.W., (2001). A Streptococcus pneumoniae pathogenicity island encoding an ABC transporter involved in iron uptake and virulence. *MolMicrobiol* **40**, *572-585*, *https://doi.org/DOI* 10.1046/j.1365-2958.2001.02414.x.

[21] Ge, R., Sun, X., (2014). Iron acquisition and regulation systems in Streptococcus species. *Metallomics*, **6**, *996-1003*, *https://doi.org/10.1039/c4mt00011k*.

[22] Tai, S.S., Yu, C., Lee, J.K., (2003). A solute binding protein of Streptococcus pneumoniae iron transport. *FEMS Microbiol Lett*, **220**, *303-308*,

[23] Miao, X., He, J., Zhang, L., Zhao, X., Ge, R., He, Q.Y., Sun, X., (2018). A Novel Iron Transporter SPD_1590 in *Streptococcus pneumoniae* Contributing to Bacterial Virulence Properties. *Front Microbiol*, **9**, *1624*, https://doi.org/10.3389/fmicb.2018.01624.

[24] Yang, X.Y., He, K., Du, G., Wu, X., Yu, G., Pan, Y., Zhang, G., Sun, X., He, Q.Y., (2016). Integrated Translatomics with Proteomics to Identify Novel Iron-Transporting Proteins in *Streptococcus pneumoniae*. *Front Microbiol*, **7**, *78*, https://doi.org/10.3389/fmicb.2016.00078.

[25] Cheng, W., Li, Q., Jiang, Y.L., Zhou, C.Z., Chen, Y., (2013). Structures of Streptococcus pneumoniae PiaA and its complex with ferrichrome reveal insights into the substrate binding and release of high affinity iron transporters. *PLoS One*, **8**, *e71451*, https://doi.org/10.1371/journal.pone.0071451.

[26] Gonzales, X.F., Castillo-Rojas, G., Castillo-Rodal, A.I., Tuomanen, E., Lopez-Vidal, Y., (2013). Catecholamine norepinephrine diminishes lung epithelial cell adhesion of Streptococcus pneumoniae by binding iron. *Microbiology*, **159**, *2333-2341*, https://doi.org/10.1099/mic.0.065607-0.

[27] Sandrini, S., Alghofaili, F., Freestone, P., Yesilkaya, H., (2014). Host stress hormone norepinephrine stimulates pneumococcal growth, biofilm formation and virulence gene expression. *BMC Microbiol*, **14**, *180*, https://doi.org/10.1186/1471-2180-14-180.

[28] Sandrini, S.M., Shergill, R., Woodward, J., Muralikuttan, R., Haigh, R.D., Lyte, M., Freestone, P.P., (2010). Elucidation of the mechanism by which catecholamine stress hormones liberate iron from the innate immune defense proteins transferrin and lactoferrin. *J Bacteriol*, **192**, *587-594*, https://doi.org/10.1128/JB.01028-09.

[29] O'Donnell, P.M., Aviles, H., Lyte, M., Sonnenfeld, G., (2006). Enhancement of in vitro growth of pathogenic bacteria by norepinephrine: importance of inoculum density and role of transferrin. *Appl Environ Microbiol*, **72**, *5097-5099*, https://doi.org/10.1128/AEM.00075-06.

[30] Beasley, F.C., Marolda, C.L., Cheung, J., Buac, S., Heinrichs, D.E., (2011). *Staphylococcus aureus* transporters Hts, Sir, and Sst capture iron liberated from human transferrin by Staphyloferrin A, Staphyloferrin B, and catecholamine stress hormones, respectively, and contribute to virulence. *Infect Immun*, **79**, *2345-2355*, https://doi.org/10.1128/IAI.00117-11.

[31] Berntsson, R.P., Smits, S.H., Schmitt, L., Slotboom, D.J., Poolman, B., (2010). A structural classification of substrate-binding proteins. *FEBS Lett*, **584**, *2606-2617*, https://doi.org/10.1016/j.febslet.2010.04.043.

[32] Dintilhac, A., Claverys, J.P., (1997). The adc locus, which affects competence for genetic transformation in *Streptococcus pneumoniae*, encodes an ABC transporter with a putative lipoprotein homologous to a family of streptococcal adhesins. *Res Microbiol*, **148**, *119-131*,

[33] Dintilhac, A., Alloing, G., Granadel, C., Claverys, J.P., (1997). Competence and virulence of *Streptococcus pneumoniae*: Adc and PsaA mutants exhibit a requirement for Zn and Mn resulting from inactivation of putative ABC metal permeases. *Mol Microbiol*, **25**, *727-739*,

[34] Pinkett, H.W., Lee, A.T., Lum, P., Locher, K.P., Rees, D.C., (2007). An inward-facing conformation of a putative metal-chelate-type ABC transporter. *Science*, **315**, *373-377*,

[35] Locher, K.P., Lee, A.T., Rees, D.C., (2002). The E. coli BtuCD structure: a framework for ABC transporter architecture and mechanism. *Science*, **296**, *1091-1098*,

[36] Naoe, Y., Nakamura, N., Doi, A., Sawabe, M., Nakamura, H., Shiro, Y., Sugimoto, H., (2016). Crystal structure of bacterial haem importer complex in the inward-facing conformation. *Nat Commun*, **7**, *13411*, *https://doi.org/10.1038/ncomms13411*.

[37] Qasem-Abdullah, H., Perach, M., Livnat-Levanon, N., Lewinson, O., (2017). ATP binding and hydrolysis disrupt the high-affinity interaction between the heme ABC transporter HmuUV and its cognate substrate-binding protein. *J Biol Chem*, **292**, *14617-14624*, *https://doi.org/10.1074/jbc.M117.779975*.

[38] de Boer, M., Gouridis, G., Vietrov, R., Begg, S.L., Schuurman-Wolters, G.K., Husada, F., Eleftheriadis, N., Poolman, B., McDevitt, C.A., Cordes, T., (2019). Conformational and dynamic plasticity in substrate-binding proteins underlies selective transport in ABC importers. *Elife*, **8**, *44652*, *https://doi.org/10.7554/eLife.44652*.

[39] Lewinson, O., Livnat-Levanon, N., (2017). Mechanism of Action of ABC Importers: Conservation, Divergence, and Physiological Adaptations. *J Mol Biol*, **429**, *606-619*, *https://doi.org/10.1016/j.jmb.2017.01.010*.

[40] Tai, S.S., Lee, C.J., Winter, R.E., (1993). Hemin utilization is related to virulence of Streptococcus pneumoniae. *Infect Immun*, **61**, *5401-5405*,

[41] Raines, D.J., Moroz, O.V., Blagova, E.V., Turkenburg, J.P., Wilson, K.S., Duhme-Klair, A.K., (2016). Bacteria in an intense competition for iron: Key component of the Campylobacter jejuni iron uptake system scavenges enterobactin hydrolysis product. *Proc Natl Acad Sci U S A*, **113**, *5850-5855*, *https://doi.org/10.1073/pnas.1520829113*.

[42] Wilde, E.J., Hughes, A., Blagova, E.V., Moroz, O.V., Thomas, R.P., Turkenburg, J.P., Raines, D.J., Duhme-Klair, A.K., Wilson, K.S., (2017). Interactions of the periplasmic binding protein CeuE with Fe(III) n-LICAM(4-) siderophore analogues of varied linker length. *Sci Rep*, **7**, *45941*, *https://doi.org/10.1038/srep45941*.

[43] Wilde, E.J., Blagova, E.V., Sanderson, T.J., Raines, D.J., Thomas, R.P., Routledge, A., Duhme-Klair, A.K., Wilson, K.S., (2019). Mimicking salmochelin S1 and the interactions of its Fe(III) complex with periplasmic iron siderophore binding proteins CeuE and VctP. *J Inorg Biochem*, **190**, *75-84*, *https://doi.org/10.1016/j.jinorgbio.2018.10.008*.

[44] Delepelaire, P., (2019). Bacterial ABC transporters of iron containing compounds. *Res Microbiol*, **170**, *345-357*, *https://doi.org/10.1016/j.resmic.2019.10.008*.

[45] Raines, D.J., Moroz, O.V., Wilson, K.S., Duhme-Klair, A.K., (2013). Interactions of a Periplasmic Binding Protein with a Tetradentate Siderophore Mimic. *Angew Chem Inter Ed*, **52**, *4595-4598*, *https://doi.org/10.1002/anie.201300751*.

[46] Chu, B.C., Otten, R., Krewulak, K.D., Mulder, F.A., Vogel, H.J., (2014). The solution structure, binding properties, and dynamics of the bacterial siderophore-binding protein FepB. *J Biol Chem*, **289**, *29219-29234*, *https://doi.org/10.1074/jbc.M114.564021*.

[47] Li, H., Sadler, P.J., Sun, H., (1996). Rationalization of the strength of metal binding to human serum transferrin. *Eur J Biochem*, **242**, *387-393*, *https://doi.org/10.1111/j.1432-1033.1996.0387r.x*.

[48] Edmonds, K.A., Zhang, Y., Raines, D.J., Duhme-Klair, A.K., Giedroc, D.P., (2020). 1H, 13C, 15N backbone resonance assignments of the apo and holo forms of the ABC transporter solute binding protein PiuA from *Streptococcus pneumoniae*. *Biomol NMR Assign*, *in the press*, *https://doi.org/10.1007/s12104-020-09952-9*.

[49] Zawadzka, A.M., Kim, Y., Maltseva, N., Nichiporuk, R., Fan, Y., Joachimiak, A., Raymond, K.N., (2009). Characterization of a Bacillus subtilis transporter for petrobactin, an anthrax stealth siderophore. *Proc Natl Acad Sci U S A*, **106**, *21854-21859*, *https://doi.org/10.1073/pnas.0904793106*.

[50] Waterhouse, A., Bertoni, M., Bienert, S., Studer, G., Tauriello, G., Gumienny, R., Heer, F.T., de Beer, T.A.P., Rempfer, C., Bordoli, L., Lepore, R., Schwede, T., (2018).

SWISS-MODEL: homology modelling of protein structures and complexes. *Nucleic Acids Res*, **46**, *W296-W303*, https://doi.org/10.1093/nar/gky427.

[51] PDB:4JCC. https://doi.org/DOI:10.2210/pdb4jcc/pdb.

[52] Garcia de la Torre, J., Huertas, M.L., Carrasco, B., (2000). HYDRONMR: prediction of NMR relaxation of globular proteins from atomic-level structures and hydrodynamic calculations. *J Magn Reson*, **147**, *138-146*, https://doi.org/10.1006/jmre.2000.2170.

[53] Hwang, P.M., Skrynnikov, N.R., Kay, L.E., (2001). Domain orientation in beta-cyclodextrin-loaded maltose binding protein: diffusion anisotropy measurements confirm the results of a dipolar coupling study. *J Biomol NMR*, **20**, *83-88*, https://doi.org/10.1023/a:1011226512421.

[54] Capdevila, D.A., Huerta, F., Edmonds, K.A., Le, M.T., Wu, H., Giedroc, D.P., (2018). Tuning site-specific dynamics to drive allosteric activation in a pneumococcal zinc uptake regulator. *Elife*, **7**, *37268*, https://doi.org/10.7554/eLife.37268.

[55] Navati, M.S., Samuni, U., Aisen, P., Friedman, J.M., (2003). Binding and release of iron by gel-encapsulated human transferrin: Evidence for a conformational search. *Proc Natl Acad Sci U S A*, **100**, *3832-3837*, https://doi.org/10.1073/pnas.262526399.

[56] Charkoudian, L.K., Franz, K.J., (2006). Fe(III)-coordination properties of neuromelanin components: 5,6-dihydroxyindole and 5,6-dihydroxyindole-2-carboxylic acid. *Inorg Chem*, **45**, *3657-3664*, https://doi.org/10.1021/ic060014r.

[57] Slager, J., Aprianto, R., Veening, J.W., (2018). Deep genome annotation of the opportunistic human pathogen Streptococcus pneumoniae D39. *Nucleic Acids Res*, **46**, *9971-9989*, https://doi.org/10.1093/nar/gky725.

[58] Thompson, J.P., Boyle, J.R., Thompson, M.M., Strupish, J., Bell, P.R., Smith, G., (1999). Cardiovascular and catecholamine responses during endovascular and conventional abdominal aortic aneurysm repair. *Eur J Vasc Endovasc Surg*, **17**, *326-333*,

[59] Esler, M., Jennings, G., Korner, P., Blombery, P., Sacharias, N., Leonard, P., (1984). Measurement of total and organ-specific norepinephrine kinetics in humans. *Am J Physiol*, **247**, *E21-28*, https://doi.org/10.1152/ajpendo.1984.247.1.E21.

[60] Gonzales, X.F., Castillo-Rojas, G., Castillo-Rodal, A.I., Tuomanen, E., Lopez-Vidal, Y., (2013). Catecholamine norepinephrine diminishes lung epithelial cell adhesion of Streptococcus pneumoniae by binding iron. *Microbiology*, **159**, *2333-2341*, https://doi.org/10.1099/mic.0.065607-0.

[61] Freestone, P.P., Haigh, R.D., Williams, P.H., Lyte, M., (2003). Involvement of enterobactin in norepinephrine-mediated iron supply from transferrin to enterohaemorrhagic Escherichia coli. *FEMS Microbiol Lett*, **222**, *39-43*, https://doi.org/10.1016/S0378-1097(03)00243-X.

[62] Zhang, Y., Sen, S., Giedroc, D.P., (2020). Iron Acquisition by Bacterial Pathogens: Beyond Tris-Catecholate Complexes. *Chembiochem*, **21**, 1955-1967 https://doi.org/10.1002/cbic.201900778.

[63] Rabsch, W., Methner, U., Voigt, W., Tschape, H., Reissbrodt, R., Williams, P.H., (2003). Role of receptor proteins for enterobactin and 2,3-dihydroxybenzoylserine in virulence of *Salmonella enterica*. *Infect Immun*, **71**, *6953-6961*, https://doi.org/10.1128/iai.71.12.6953-6961.2003.

[64] Zeng, X., Xu, F., Lin, J., (2013). Specific TonB-ExbB-ExbD energy transduction systems required for ferric enterobactin acquisition in Campylobacter. *FEMS Microbiol Lett*, **347**, *83-91*, https://doi.org/10.1111/1574-6968.12221.

[65] Zeng, X., Mo, Y., Xu, F., Lin, J., (2013). Identification and characterization of a periplasmic trilactone esterase, Cee, revealed unique features of ferric enterobactin acquisition in Campylobacter. *Mol Microbiol*, **87**, *594-608*, https://doi.org/10.1111/mmi.12118.

[66] Xu, F., Zeng, X., Haigh, R.D., Ketley, J.M., Lin, J., (2010). Identification and characterization of a new ferric enterobactin receptor, CfrB, in Campylobacter. *J Bacteriol*, **192**, *4425-4435*, *https://doi.org/10.1128/JB.00478-10*.

[67] Zeng, X., Xu, F., Lin, J., (2009). Molecular, antigenic, and functional characteristics of ferric enterobactin receptor CfrA in *Campylobacter jejuni. Infect Immun*, **77**, *5437-5448*, *https://doi.org/10.1128/IAI.00666-09*.

[68] Crouch, M.L., Castor, M., Karlinsey, J.E., Kalhorn, T., Fang, F.C., (2008). Biosynthesis and IroC-dependent export of the siderophore salmochelin are essential for virulence of Salmonella enterica serovar Typhimurium. *Mol Microbiol*, **67**, *971-983*, *https://doi.org/10.1111/j.1365-2958.2007.06089.x*.

[69] Xu, Q., Pichichero, M.E., (2014). Co-colonization by Haemophilus influenzae with Streptococcus pneumoniae enhances pneumococcal-specific antibody response in young children. *Vaccine*, **32**, *706-711*, *https://doi.org/10.1016/j.vaccine.2013.11.096*.

[70] Anderson, D.S., Adhikari, P., Nowalk, A.J., Chen, C.Y., Mietzner, T.A., (2004). The hFbpABC transporter from Haemophilus influenzae functions as a binding-protein-dependent ABC transporter with high specificity and affinity for ferric iron. *J Bacteriol*, **186**, *6220-6229*, *https://doi.org/10.1128/JB.186.18.6220-6229.2004*.

[71] Campagnari, A.A., Shanks, K.L., Dyer, D.W., (1994). Growth of Moraxella catarrhalis with human transferrin and lactoferrin: expression of iron-repressible proteins without siderophore production. *Infect Immun*, **62**, *4909-4914*,

[72] Uranga, C.C., Arroyo, P., Jr., Duggan, B.M., Gerwick, W.H., Edlund, A., (2020). Commensal Oral Rothia mucilaginosa Produces Enterobactin, a Metal-Chelating Siderophore. *mSystems*, **5**, *https://doi.org/10.1128/mSystems.00161-20*.

[73] Pi, H., Helmann, J.D., (2018). Genome-wide characterization of the Fur regulatory network reveals a link between catechol degradation and bacillibactin metabolism in *Bacillus subtilis. mBio*, **9**, e01451-18. *https://doi: 10.1128/mBio.01451-18*.

[74] Schweigert, N., Hunziker, R.W., Escher, B.I., Eggen, R.I., (2001). Acute toxicity of (chloro-)catechols and (chloro-)catechol-copper combinations in Escherichia coli corresponds to their membrane toxicity in vitro. *Environ Toxicol Chem*, **20**, *239-247*,

[75] Monks, T.J., Lau, S.S., (1992). Toxicology of quinone-thioethers. *Crit Rev Toxicol*, **22**, *243-270*, *https://doi.org/10.3109/10408449209146309*.

[76] Schweigert, N., Zehnder, A.J.B., Eggen, R.I.L., (2001). Chemical properties of catechols and their molecular modes of toxic action in cells, from microorganisms to mammals. *Environ Microbiol*, **3**, *81-91*, *https://doi.org/DOI* 10.1046/j.1462-2920.2001.00176.x.

[77] Schweigert, N., Acero, J.L., von Gunten, U., Canonica, S., Zehnder, A.J., Eggen, R.I., (2000). DNA degradation by the mixture of copper and catechol is caused by DNA-copper-hydroperoxo complexes, probably DNA-Cu(I)OOH. *Environ Mol Mutagen*, **36**, *5-12*,

[78] Counago, R.M., Ween, M.P., Begg, S.L., Bajaj, M., Zuegg, J., O'Mara, M.L., Cooper, M.A., McEwan, A.G., Paton, J.C., Kobe, B., McDevitt, C.A., (2014). Imperfect coordination chemistry facilitates metal ion release in the Psa permease. *Nat Chem Biol*, **10**, *35-41*, *https://doi.org/10.1038/nchembio.1382*.

[79] Deplazes, E., Begg, S.L., van Wonderen, J.H., Campbell, R., Kobe, B., Paton, J.C., MacMillan, F., McDevitt, C.A., O'Mara, M.L., (2015). Characterizing the conformational dynamics of metal-free PsaA using molecular dynamics simulations and electron paramagnetic resonance spectroscopy. *Biophys Chem*, **207**, *51-60*, *https://doi.org/10.1016/j.bpc.2015.08.004*.

[80] Peuckert, F., Miethke, M., Albrecht, A.G., Essen, L.O., Marahiel, M.A., (2009). Structural basis and stereochemistry of triscatecholate siderophore binding by FeuA. *Angew Chem Int Ed Engl*, **48**, *7924-7927*, *https://doi.org/10.1002/anie.200902495*.

[81] de Boer, M., Gouridis, G., Muthahari, Y.A., Cordes, T., (2019). Single-Molecule Observation of Ligand Binding and Conformational Changes in FeuA. *Biophys J*, **117**, *1642-1654*, *https://doi.org/10.1016/j.bpj.2019.08.005*.

[82] Hvorup, R.N., Goetz, B.A., Niederer, M., Hollenstein, K., Perozo, E., Locher, K.P., (2007). Asymmetry in the structure of the ABC transporter-binding protein complex BtuCD-BtuF. *Science*, **317**, *1387-1390*, *https://doi.org/10.1126/science.1145950*.

[83] Lanie, J.A., Ng, W.L., Kazmierczak, K.M., Andrzejewski, T.M., Davidsen, T.M., Wayne, K.J., Tettelin, H., Glass, J.I., Winkler, M.E., (2007). Genome sequence of Avery's virulent serotype 2 strain D39 of Streptococcus pneumoniae and comparison with that of unencapsulated laboratory strain R6. *J Bacteriol*, **189**, *38-51*,

[84] Peroutka, R.J., Elshourbagy, N., Piech, T., Butt, T.R., (2008). Enhanced protein expression in mammalian cells using engineered SUMO fusions: secreted phospholipase A2. *Protein Sci*, **17**, *1586-1595*, *https://doi.org/10.1110/ps.035576.108*.

[85] Ramirez, R.J.A., Karamanukyan, L., Ortiz, S., Gutierrez, C.G., (1997). A much improved synthesis of the siderophore enterobactin. *Tetrahedron Letters*, **38**, *749-752*,

[86] Nolan, E.M., Fischbach, M.A., Koglin, A., Walsh, C.T., (2007). Biosynthetic tailoring of microcin E492m: post-translational modification affords an antibacterial siderophore-peptide conjugate. *J Am Chem Soc*, **129**, *14336-14347*, *https://doi.org/10.1021/ja074650f*.

[87] Duhme, A.-K., Dauter, Z., Hider, R.C., Pohl, S., (1996). Complexation of Molybdenum by Siderophores: Synthesis and Structure of the Double-Helical cis-Dioxomolybdenum(VI) Complex of a Bis(catecholamide) Siderophore Analogue. *Inorg Chem*, **35**, *3059-3061*, *https://doi.org/https://doi.org/10.1021/ic9512183*.

[88] Weitl, F.L., Raymond, K.N., (1980). Specific sequestering agents for the actinides. 3. Polycatecholate ligands derived from 2,3-dihydroxy-5-sulfobenzoyl conjugates of diaza- and tetraazaalkanes. *J Am Chem Soc*, **102**, *2289-2293*, *https://doi.org/https://doi.org/10.1021/ja00527a026*.

[89] Maciejewski, M.W., Schuyler, A.D., Gryk, M.R., Moraru, II, Romero, P.R., Ulrich, E.L., Eghbalnia, H.R., Livny, M., Delaglio, F., Hoch, J.C., (2017). NMRbox: A Resource for Biomolecular NMR Computation. *Biophys J*, **112**, *1529-1534*, *https://doi.org/10.1016/j.bpj.2017.03.011*.

[90] Delaglio, F., Grzesiek, S., Vuister, G.W., Zhu, G., Pfeifer, J., Bax, A., (1995). NMRPipe: a multidimensional spectral processing system based on UNIX pipes. *J Biomol NMR*, **6**, *277-293*,

[91] Lee, W., Tonelli, M., Markley, J.L., (2015). NMRFAM-SPARKY: enhanced software for biomolecular NMR spectroscopy. *Bioinformatics*, **31**, *1325-1327*, *https://doi.org/10.1093/bioinformatics/btu830*.

[92] Schneidman-Duhovny, D., Hammel, M., Tainer, J.A., Sali, A., (2013). Accurate SAXS profile computation and its assessment by contrast variation experiments. *Biophys J*, **105**, *962-974*, *https://doi.org/10.1016/j.bpj.2013.07.020*.

[93] Schneidman-Duhovny, D., Hammel, M., Tainer, J.A., Sali, A., (2016). FoXS, FoXSDock and MultiFoXS: Single-state and multi-state structural modeling of proteins and their complexes based on SAXS profiles. *Nucleic Acids Res*, **44**, *W424-429*, *https://doi.org/10.1093/nar/gkw389*.

[94] Guex, N., Peitsch, M.C., Schwede, T., (2009). Automated comparative protein structure modeling with SWISS-MODEL and Swiss-PdbViewer: a historical perspective. *Electrophoresis*, **30 Suppl 1**, *S162-173*, *https://doi.org/10.1002/elps.200900140*.

[95] Bienert, S., Waterhouse, A., de Beer, T.A., Tauriello, G., Studer, G., Bordoli, L., Schwede, T., (2017). The SWISS-MODEL Repository-new features and functionality. *Nucleic Acids Res*, **45**, *D313-D319*, *https://doi.org/10.1093/nar/gkw1132*.

[96]   Studer, G., Rempfer, C., Waterhouse, A.M., Gumienny, R., Haas, J., Schwede, T., (2020). QMEANDisCo-distance constraints applied on model quality estimation. *Bioinformatics*, **36**, *2647*, *https://doi.org/10.1093/bioinformatics/btaa058*.

[97]   Frieden, E., Aisen, P., (1980). Forms of Iron Transferrin. *Trends Biochem Sci*, **5**, *R11-R11*,

[98]   Turcot, I., Stintzi, A., Xu, J., Raymond, K.N., (2000). Fast biological iron chelators: kinetics of iron removal from human diferric transferrin by multidentate hydroxypyridonates. *J Biol Inorg Chem*, **5**, *634-641*, *https://doi.org/10.1007/s007750000149*.

[99]   Aisen, P., Leibman, A., (1972). Lactoferrin and transferrin: a comparative study. *Biochim Biophys Acta*, **257**, *314-323*, *https://doi.org/10.1016/0005-2795(72)90283-8*.

[100] Zhu, G., Xia, Y., Nicholson, L.K., Sze, K.H., (2000). Protein dynamics measurements by TROSY-based NMR experiments. *J Magn Reson*, **143**, *423-426*, *https://doi.org/10.1006/jmre.2000.2022*.

[101] Cho, C.H., Urquidi, J., Singh, S., Robinson, G.W., (1999). Thermal offset viscosities of liquid H2O, D2O, and T2O. *J Phys Chem B*, **103**, *1991-1994*, *https://doi.org/DOI 10.1021/jp9842953*.

[102] Tollinger, M., Skrynnikov, N.R., Mulder, F.A.A., Forman-Kay, J.D., Kay, L.E., (2001). Slow dynamics in folded and unfolded states of an SH3 domain. *J Am Chem Soc*, **123**, *11341-11352*, *https://doi.org/10.1021/ja011300z*.

[103] Korzhnev, D.M., Kloiber, K., Kanelis, V., Tugarinov, V., Kay, L.E., (2004). Probing slow dynamics in high molecular weight proteins by methyl-TROSY NMR spectroscopy: application to a 723-residue enzyme. *J Am Chem Soc*, **126**, *3964-3973*, *https://doi.org/10.1021/ja039587i*.

[104] Sievers, F., Wilm, A., Dineen, D., Gibson, T.J., Karplus, K., Li, W., Lopez, R., McWilliam, H., Remmert, M., Soding, J., Thompson, J.D., Higgins, D.G., (2011). Fast, scalable generation of high-quality protein multiple sequence alignments using Clustal Omega. *Mol Syst Biol*, **7**, *539*, *https://doi.org/10.1038/msb.2011.75*.

[105] Robert, X., Gouet, P., (2014). Deciphering key features in protein structures with the new ENDscript server. *Nucleic Acids Res*, **42**, *W320-324*, *https://doi.org/10.1093/nar/gku316*.

TABLES

Table 1. Binding affinities (K_a, M^{-1}) for the binding of *S. pneumoniae* PiuA and *S. aureus* SstD to various Fe^{III} coordination complexes[a]

K_a (M^{-1})	PiuA			SstD		
	WT	H238L	Y300F	WT	H260L	Y321F
hemin	$2.3{\pm}0.4 \times 10^6$			$2.2{\pm}0.2 \times 10^6$		
Fe^{III}–4-LICAM	$\geq 1.0 \times 10^{9\ b}$	$1.3{\pm}0.1 \times 10^7$	$3.7{\pm}0.6 \times 10^6$	$\geq 1.0 \times 10^{9\ b}$	$1.0{\pm}0.1 \times 10^7$	$2.0{\pm}0.3 \times 10^6$
Fe^{III}–Ent	$2.6{\pm}0.2 \times 10^6$			$2.0{\pm}0.2 \times 10^6$		
Fe^{III}–di-DHBS	$\geq 1.0 \times 10^{9\ b}$	$1.2{\pm}0.3 \times 10^8$	$2.6{\pm}0.3 \times 10^6$	$\geq 1.0 \times 10^{9\ b}$	$2.2{\pm}1.2 \times 10^8$	$1.1{\pm}0.3 \times 10^6$
Fe^{III}–DHBS$_2$	$\geq 1.0 \times 10^{9\ b}$	$2.5{\pm}0.4 \times 10^8$	$2.7{\pm}0.2 \times 10^6$	$\geq 1.0 \times 10^{9\ b}$	$1.6{\pm}0.5 \times 10^8$	$4.8{\pm}0.8 \times 10^6$
Fe^{III}–NE$_2$	$\geq 1.0 \times 10^{9\ b}$	$6.0{\pm}3.5 \times 10^7$	$9.5{\pm}3.6 \times 10^6$	$\geq 1.0 \times 10^{9\ b}$	$3.0{\pm}0.9 \times 10^7$	$1.1{\pm}0.4 \times 10^7$
Fe^{III}–6FNE$_2$	$\geq 1.0 \times 10^{9\ b}$					
Ga^{III}–4-LICAM	$1.0{\pm}0.2 \times 10^8$					

[a]Conditions: 0.2 µM protein, 50 mM HEPES, pH 7.5, 150 mM NaCl, 25.0 ºC. [b]The K_a indicated represents a lower limit (stoichiometric binding).

Table 2. Relative masses and average masses (observed and expected) for major species observed by native state ESI-MS[a]

	z=11		z=12		Observed		Expected	
	m/z	Δm/z	m/z	Δm/z	Avg. Mass (Da)	Δmass (Da)	avg mass (Da)	Δmass (Da)
apo PiuA	2852.2	—	2620.2	—	31429.7	—	31433.8	—
Fe^{III}–4-LICAM PiuA	2895.6	37.4	2654.6	34.4	31841.8	412.1	31844.0	412.1
Fe^{III}–NE$_2$ PiuA	2893.6	35.5	2652.7	32.4	31819.5	389.8	31822.2	390.4
Fe^{III}–NE PiuA	2878.2	20.0	2638.6	18.4	31650.1	220.4	31653.1	223.2
Fe^{III}–NE-Ac PiuA	2884.0	25.8	2643.9	23.6	31713.3	283.5	31716.1	282.2

[a] Mass spectra (z=12) shown in Fig. 3A. Δm/z and Δmass correspond to the mass differences between the indicated species and the unliganded (apo) PiuA (top entry).
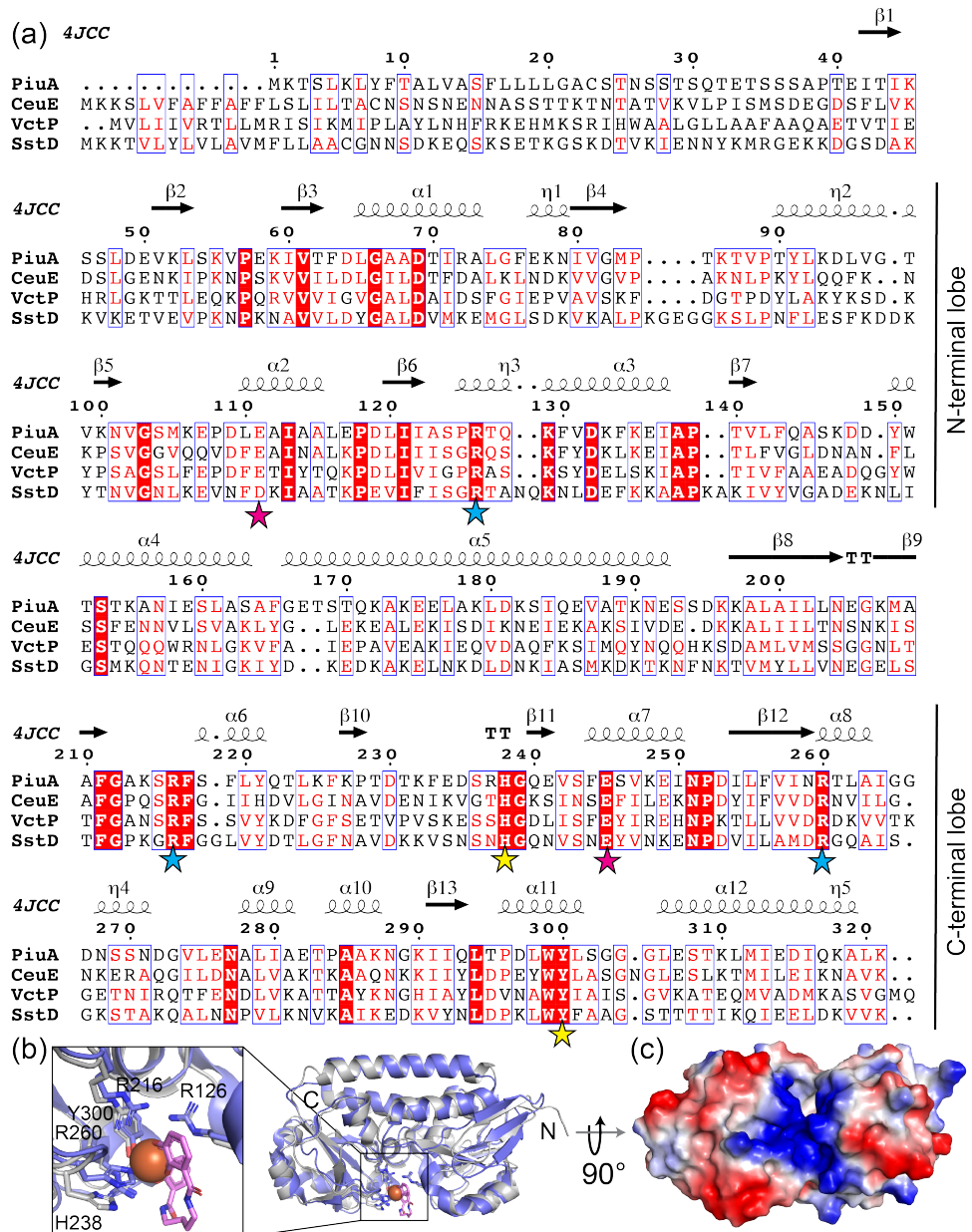
Fig. 1. Structural characteristics of *Streptococcus pneumoniae* D39 PiuA. (a) Sequence alignment of PiuA with CeuE, VctP, and SstD, with secondary structure of apo PiuA from *Streptococcus pneumoniae Canada MDR_19A* shown above (PDB 4JCC). Conserved Fe[III]-binding residues and arginine residues are marked below with *yellow* and *cyan* stars, respectively. Conserved acidic residues likely to form salt bridges with the permease are marked with *magenta* stars. The alignment was performed using Clustal Omega [104] and visualized with ESPript [105]. (b) Superposition of structures of apo PiuA (*gray*) and CeuE

(*blue*) bound to Fe^{III}--4-LICAM (*orange*, *magenta*), with side chains of conserved iron- and catecholate-binding residues highlighted as sticks (PDB 5A1J) [45]. (c) Surface potential of apo PiuA (PDB 4JCC), showing a positively charged binding cleft in blue between the N- and C-terminal lobes (right and left, respectively). All structure images were rendered with PyMOL (PyMOL Molecular Graphics System, Ver. 2, Schrödinger, LLC).
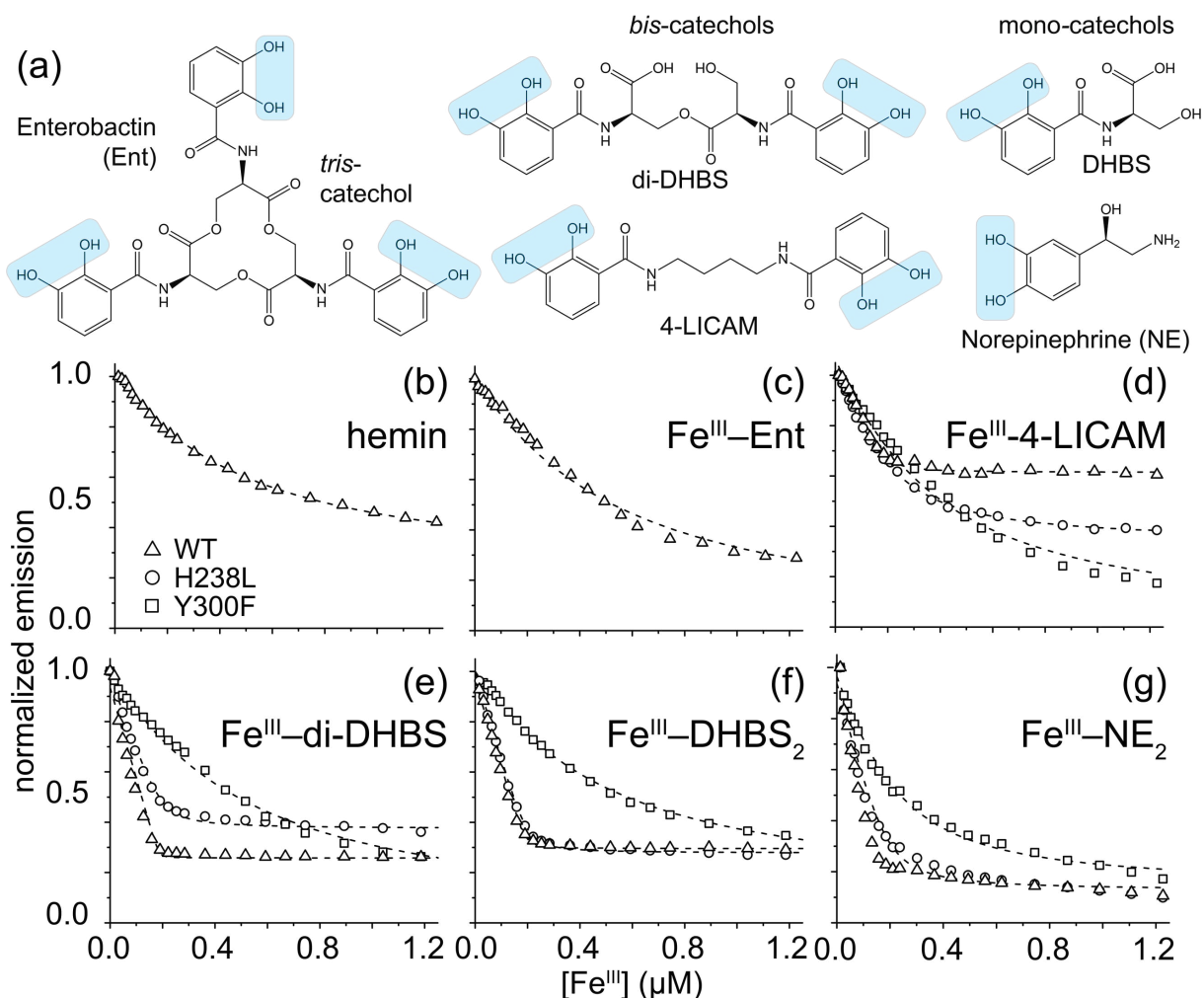
Fig 2. Ligand binding properties of PiuA. (a) *Tris-*, *bis-*, and mono-catechol ligands used in this work, with catechol moieties highlighted. (b-g) Ligand binding by wild-type PiuA (open triangles), H238L PiuA (open circles) and Y300F PiuA (open squares) as monitored by quenching of the intrinsic PiuA tryptophan fluorescence. Smooth curves drawn through the data represent the results of nonlinear squares fitting to a 1:1 PiuA:ligand binding model with the parameters compiled in Table 1. Ligands are Fe^{III} coordination complexes: (b) hemin; (c) Fe^{III}–Ent; (d) Fe^{III}–4-LICAM; (e) Fe^{III}–di-DHBS; (f) Fe^{III}–$DHBS_2$; (g) Fe^{III}–NE_2. Conditions: 0.2 μM PiuA, 50 mM HEPES, pH 7.5, 150 mM NaCl, 25.0 ºC.

41
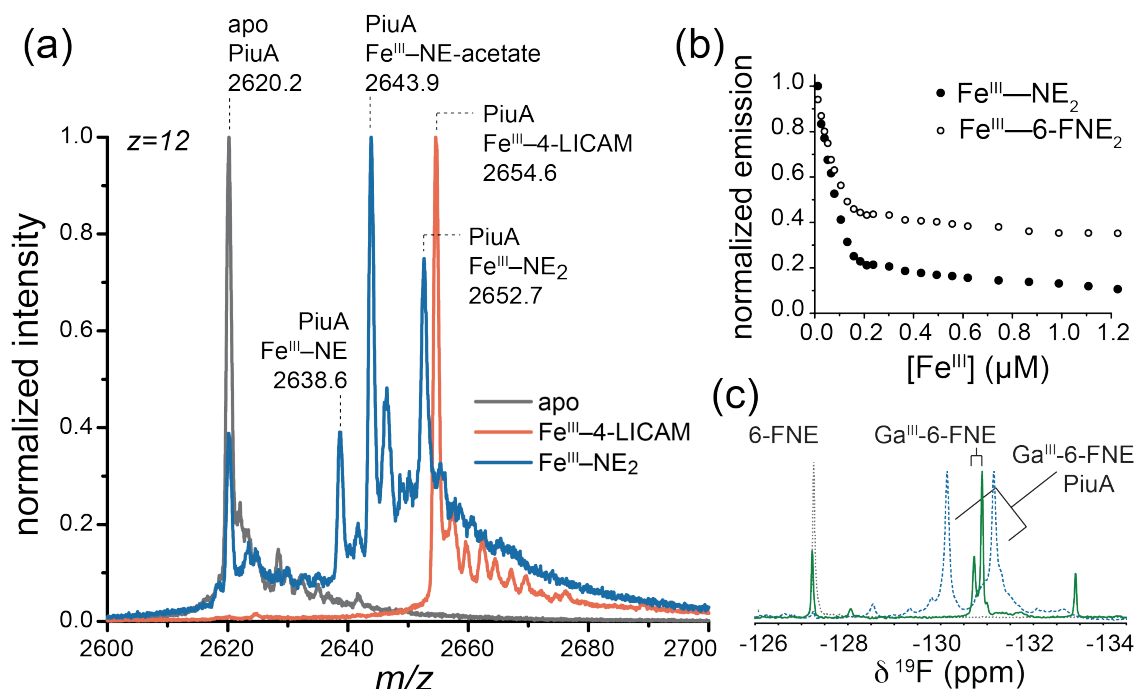
Fig. 3. Native mass spectrometry of apo-PiuA, PiuA-Fe^{III}–4-LICAM and PiuA-Fe^{III}–NE$_2$ and ^{19}F NMR analysis of Ga^{III}–6-FNE PiuA complexes. (a) Overlaid native state MS of apo-PiuA (*gray* trace), Fe^{III}–4-LICAM complex (*red* trace) and the Fe^{III}–NE$_2$ complex (*black* trace) (*z*=12 charge state). Note that some of the Fe^{III}–NE$_2$ complex dissociates into component apo, Fe^{III}–NE, Fe^{III}–NE-acetate complexes as indicated. Measured masses are shown along with expected masses in Table 2. (b) Binding curve for the Fe^{III}–6-FNE$_2$ complex vs. Fe^{III}-NE$_2$ to PiuA. Conditions: 0.2 µM PiuA, 50 mM HEPES, pH 7.5, 150 mM NaCl, 25.0 °C. (c) Overlaid ^{19}F NMR spectra of 6-FNE (*gray* dotted line) with a Ga^{III}–6-FNE$_2$ complex solution in the absence (*green* solid line) or presence (*blue* dashed line) of PiuA. Conditions: 25 mM MES pH 6.5, 150 mM NaCl, 10% v/v D$_2$O, 0.3 mM DSS, 30 µM TFA and either 0.3 mM 6-FNE alone, 0.3 mM 6-FNE with 0.35 mM GaCl$_3$, or 1 mM PiuA saturated with Ga^{III}–6-FNE.
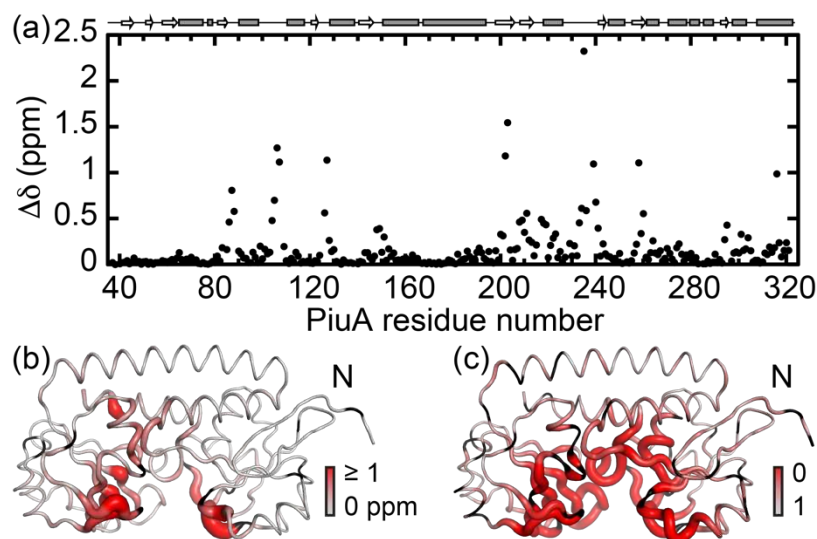
Fig. 4. ^{1}H,^{15}N NMR chemical shift perturbations (CSPs) and paramagnetic relaxation enhancement (PRE) in PiuA between the apo and bound forms. (a) Plot of CSPs upon Ga^{III}– 4-LICAM binding. (b) CSPs depicted on a tube diagram of the structure of PiuA from *S. pneumoniae* Canada MDR_19A strain (PDB 4JCC), with the largest CSPs shown as a thick tube painted *red*. The corresponding ^{1}H,^{15}N TROSY spectra are shown in Supplementary Fig. 4a,b. (c) PREs upon Fe^{III}–4-LICAM binding, depicted as peak height ratios relative to Ga^{III}–4-LICAM bound PiuA. The corresponding ^{1}H,^{15}N TROSY spectra and scatterplot are shown in Supplementary Fig. 6a,b.
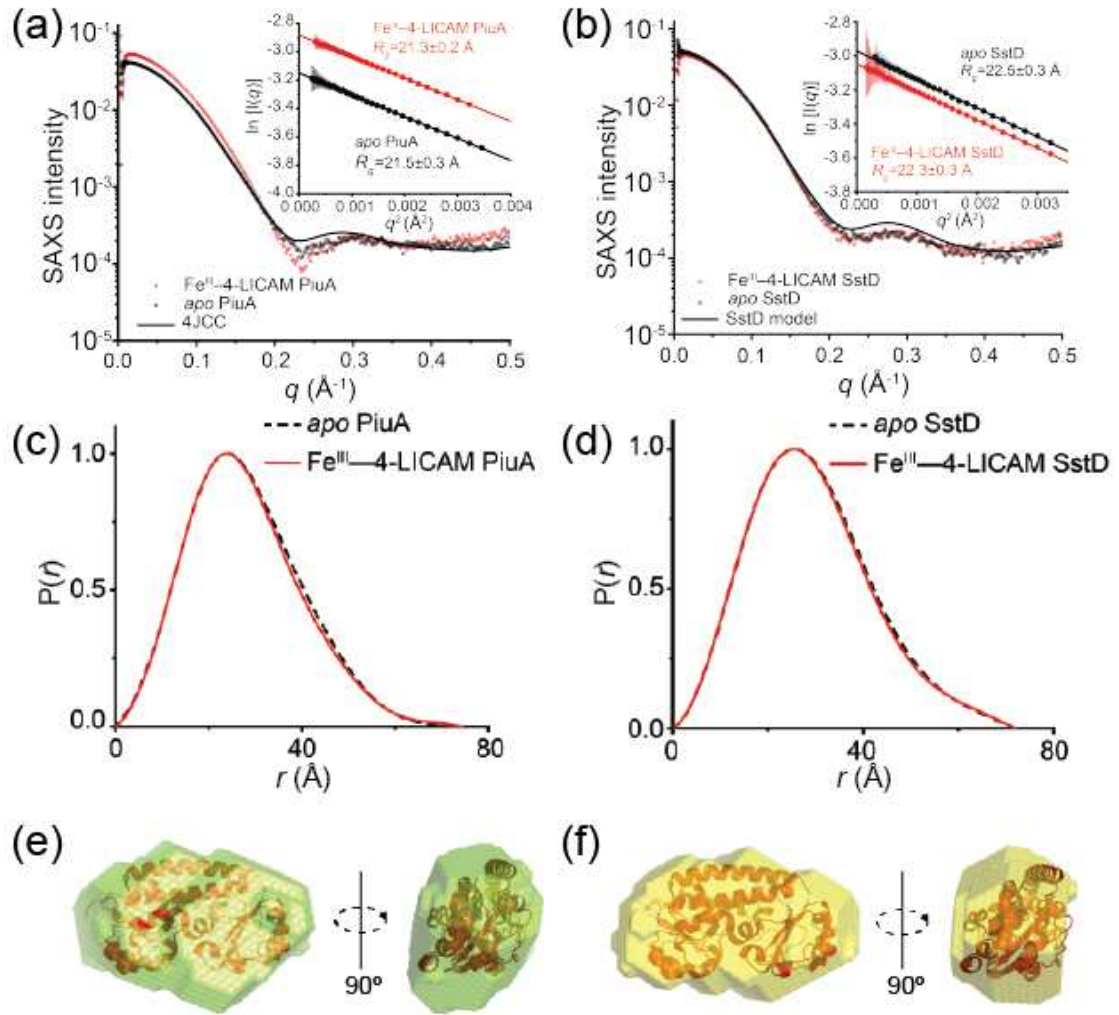
Fig. 5. Small angle x-ray scattering analysis of PiuA and SstD in apo- and ligand-bound states. (a) PiuA and (b) SstD raw SAXS plots (*gray*, apo-states; *red*, Fe^{III}–4-LICAM complex bound states) with the FoXS server-calculated SAXS scattering curves from the structural models shown for comparison (*black* line) (4JCC for apo-PiuA; SWISS MODEL structure obtained from 3GFV for apo-SstD) (main panel), and Guinier plots and linear fitting (*insets*) with R_g values shown. (c) PiuA and (d) SstD PDDF plots in the apo-state (*black* dashed line) and Fe^{III}–4-LICAM complex bound state (*red* solid line). PiuA SAXS envelope (e) of the apo state in *green* and (f) Fe^{III}–4-LICAM bound state in *yellow*, superimposed on the apo-PiuA crystal structure with PDB code: 4JCC in *red*.

44
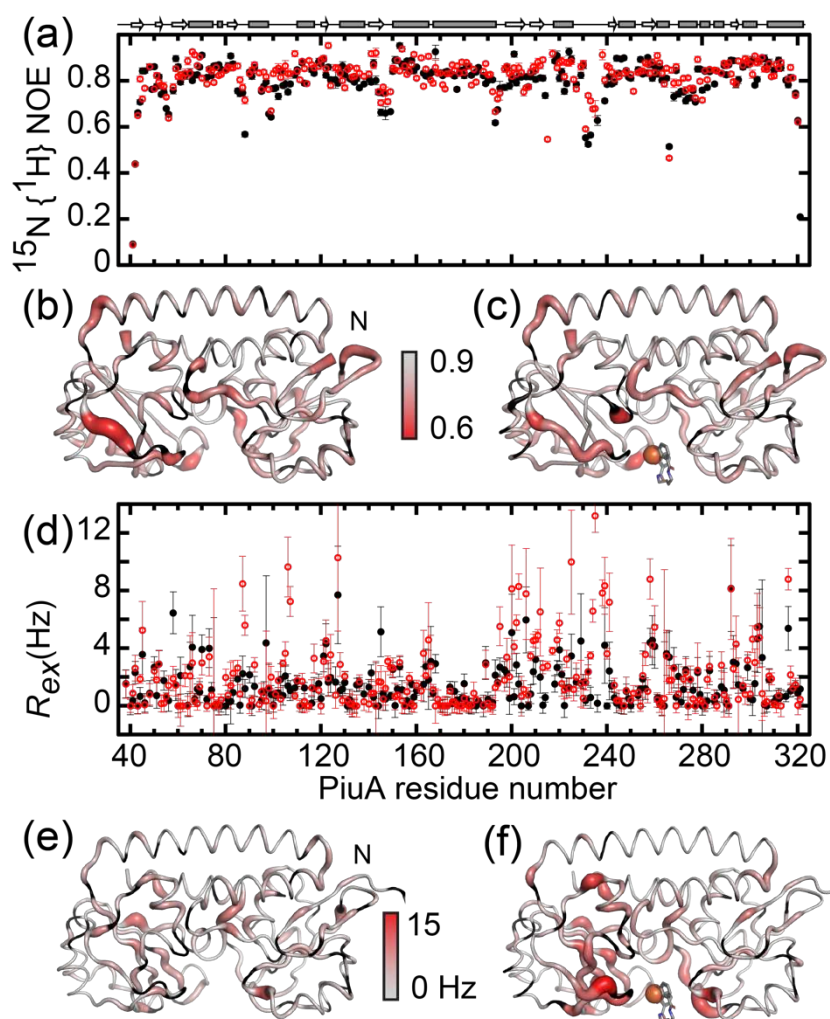
Fig. 6. Backbone dynamics of PiuA in the apo- and ligand-bound states. Steady-state heteronuclear $^{15}N\{^1H\}$ NOE (a), reporting on sub-nanosecond (sub-ns) amide bond vector motions of apo-PiuA (*black*) and PiuA bound to Ga^{III}–4-LICAM (*red*). These values are depicted on a tube diagram of the structure of PiuA from *S. pneumoniae* Canada MDR_19A strain (PDB 4JCC), with the most mobile regions shown as a thick tube painted *red*, for apo-PiuA (b) and PiuA bound to Ga^{III}–4-LICAM (c), with the substrate drawn as it appears in Fig. 1b, based on PDB 5A1J [45]. Slow timescale (μs-ms) exchange rates measured using ^{15}N relaxation dispersion experiments (d) for apo-PiuA (*black*) and PiuA bound to Ga^{III}–4-LICAM (*red*). These values are depicted on a tube diagram of the structure, with the most mobile

regions shown as a thick tube painted *red*, for apo-PiuA (e) and PiuA bound to Ga^{III}–4-LICAM (f).
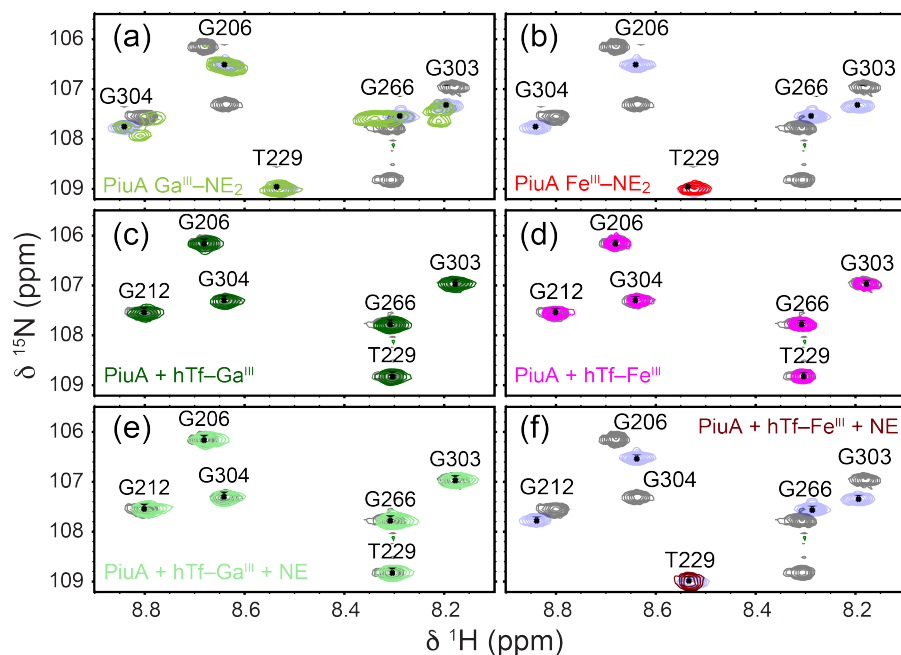
Fig. 7. NE mediates transfer of Fe^{III} from transferrin (hTf) to PiuA by NMR spectroscopy. Selected region of NMR spectra of ^{15}N PiuA showing transfer of Fe^{III} and not Ga^{III} from hTf to PiuA. (a) ^{15}N PiuA pre-loaded with Ga^{III}–NE$_2$, (b) ^{15}N PiuA pre-loaded with Fe^{III}–NE$_2$, (c) ^{15}N PiuA with Ga^{III}–hTf, showing no change, (d) ^{15}N PiuA with Fe^{III}–hTf, showing no change, (e) ^{15}N PiuA with Ga^{III}–hTf and 1 mM NE, showing no change, and (f) ^{15}N PiuA with Fe^{III}–hTf and 1 mM NE, closely resembling the spectrum shown in (b). All spectra are shown overlaid on *gray* crosspeaks corresponding to apo-PiuA. *Light blue* crosspeaks corresponding to Ga^{III}–4-LICAM are also shown in panels (a), (b), and (f) for comparison.
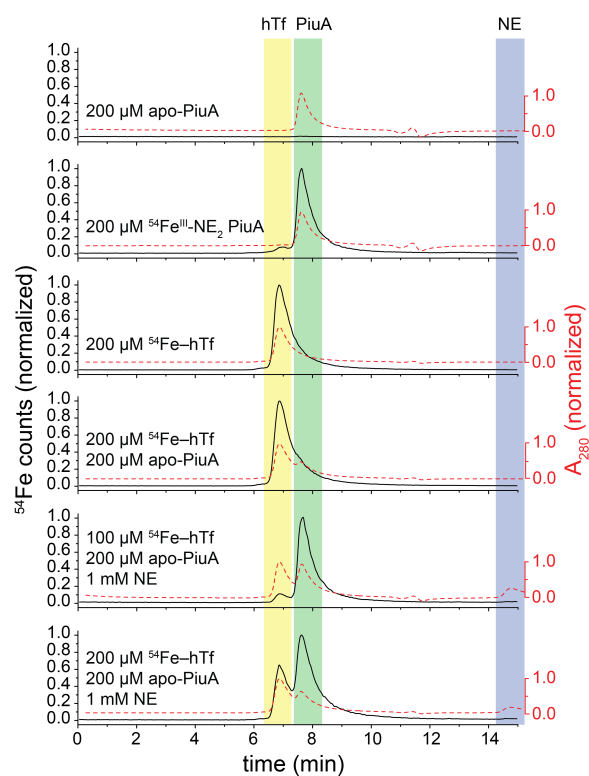
Fig. 8. Analysis of NE-dependent iron transfer from hTf to PiuA via SEC-ICP-MS. ^{54}Fe counts (left axis) of SEC-LC elution by ICP-MS plots vs. time (*black* solid line). Absorption at 280 nm (right axis) of SEC-LC elution plots vs time (*red* dashed line). Elution peaks are highlighted to show hTf (*yellow* stripe), PiuA (*green* stripe) and NE (*purple* stripe). Sample conditions prior to the chromatography are shown in each chromatogram.